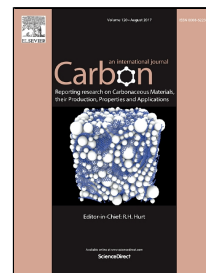


# Accepted Manuscript

Fractal nature of hard carbon prepared from C<sub>60</sub> fullerene

Damir Starešinić, Damir Dominko, Iva Šrut Rakić, Ognjen Milat, Davor Ristić, Mile Ivanda, Tea Mišić Radić, André Clément, Michel Saint-Paul, Mikhail E. Kozlov, Katica Biljaković



PII: S0008-6223(17)30701-7  
DOI: 10.1016/j.carbon.2017.07.022  
Reference: CARBON 12188  
To appear in: *Carbon*  
Received Date: 05 April 2017  
Revised Date: 02 July 2017  
Accepted Date: 08 July 2017

Please cite this article as: Damir Starešinić, Damir Dominko, Iva Šrut Rakić, Ognjen Milat, Davor Ristić, Mile Ivanda, Tea Mišić Radić, André Clément, Michel Saint-Paul, Mikhail E. Kozlov, Katica Biljaković, Fractal nature of hard carbon prepared from C<sub>60</sub> fullerene, *Carbon* (2017), doi: 10.1016/j.carbon.2017.07.022

This is a PDF file of an unedited manuscript that has been accepted for publication. As a service to our customers we are providing this early version of the manuscript. The manuscript will undergo copyediting, typesetting, and review of the resulting proof before it is published in its final form. Please note that during the production process errors may be discovered which could affect the content, and all legal disclaimers that apply to the journal pertain.

**Fractal nature of hard carbon prepared from C<sub>60</sub> fullerene**

Damir Starešinić <sup>a\*</sup>, Damir Dominko <sup>a</sup>, Iva Šrut Rakić <sup>a</sup>, Ognjen Milat <sup>a</sup>,  
Davor Ristić <sup>b</sup>, Mile Ivanda <sup>b</sup>, Tea Mišić Radić <sup>b</sup>, André Clément <sup>c</sup>,  
Michel Saint-Paul <sup>d</sup>, Mikhail E. Kozlov <sup>e</sup>, Katica Biljaković <sup>a</sup>

<sup>a</sup> Institute of Physics, Bijenička c. 46, HR-10000 Zagreb, Croatia

<sup>b</sup> Ruđer Bošković Institute, Bijenička c. 54, Hr-10000 Zagreb, Croatia

<sup>c</sup> STMicroelectronics, 12 rue J. Horowitz, 38019 Grenoble, France

<sup>d</sup> Institut NEEL, CNRS & Université Joseph Fourier, 25 Av des Martyrs, 38 042 Grenoble, France

<sup>e</sup> The University of Texas at Dallas, Chemistry/ NanoTech , 800 West Campbell Road, Richardson, Texas 75080, USA

**Abstract**

Hard form of carbon obtained by collapsing C<sub>60</sub> fullerene molecules at moderate pressure and temperature was investigated using different imaging techniques at spatial resolutions ranging from angstrom to millimeter. Hierarchical granular morphology has been observed from the atomic up to the sample size length scale, revealing scale independent grain size distribution. The unusual fractal-like structure correlates with unique transport and calorimetric properties of this material. Hard carbon can be considered as a bridge between porous and dense amorphous materials.

---

\* Corresponding author. Tel: +385 1 4498 845. E-mail: damirs@ifs.hr (Damir Starešinić)

## 1. Introduction

The ability of carbon to form  $sp$ ,  $sp^2$  and  $sp^3$  bonds with neighbors enables formation of a number of carbon allotropes such as graphite, graphene, nanotubes, fullerenes, and diamond. High mechanical hardness of cubic diamond puts this form of carbon apart making it extremely valuable for diverse machine tool applications. The market cost of diamond parts is quite high, but can be driven down by replacement of bulk crystals with much cheaper materials commonly known as diamond-like carbons (DLC) [1]. Thin DLC coatings are widely used to improve performance of cutting tools [2], but the range of their technological applications is much wider and includes, among others, scratch resistant [3], chemically inert [4] and biocompatible [5] protective coatings.

The fabrication of bulk quantities of inexpensive DLC materials with hardness comparable to that of cubic diamond still remains a technological challenge. A promising approach to the solution of this important problem is to use the metastable carbon molecules known as fullerenes [6-8] which are nowadays available in large quantities. Fullerenes, including its most common representative  $C_{60}$ , buckminsterfullerene, transform to diamond-like phase [9] under very high temperatures ( $T$ ) and pressures ( $p$ ). However, a very hard form of carbon [10] has been obtained at rather moderate conditions ( $p \sim 3$  GPa,  $T \sim 1000$  K) just outside of the region of  $C_{60}$  stability [11]. The density of this, so-called hard carbon (HC) is only slightly higher than the density of solid fullerite (molecular  $C_{60}$  solid), but its micro-hardness is comparable to that of DLC films [12]. The material is electrically conductive [10, 13] and does not reveal long range crystalline order as evidenced with X-ray diffraction, Raman [10] and NMR [14] measurements. These results suggest a partial destruction and covalent cross linking of  $C_{60}$  cages with the formation of  $sp^3$  network [10].

Thermal properties of HC, i.e. heat capacity ( $c_p$ ) [15] and thermal conductivity ( $\kappa$ ) [13, 15, 16], have  $T$  dependence characteristic for disordered systems. Fig. 1 shows  $c_p$  and  $\kappa$  of HC [15], amorphous  $SiO_2$  (a- $SiO_2$ ) [17, 18] and  $SiO_2$  aerogel [19]. At high temperatures  $c_p$  and  $\kappa$  of HC are very similar to those of a- $SiO_2$ , a typical representative of glasses. However, below  $\sim 30$  K it does not have either plateau in  $\kappa$  or a maximum in  $c_p/T^3$  (known as boson peak) which are typical for glasses. Instead, the (quasi)linear temperature dependence of  $\kappa$  extends towards much lower temperatures and  $c_p$  develops a linear contribution much higher than in glasses, which makes it more similar to aerogels [19, 20] and other porous materials [21].

The plateau in  $\kappa$  has been associated with the strong reduction of the phonon mean free path [17, 22]. In glasses the average mean free path ( $l_{mfp}$ ), which can be crudely estimated from the kinetic theory equation [23-25], falls below the wavelength of the dominant thermal phonon ( $\lambda_c$ ) [17, 24, 25] at temperatures above the plateau in  $\kappa$  [17]. This can be regarded as the Ioffe-Regel (IR) crossover for phonons [22]. The value of  $l_{mfp}$  at IR crossover of several nm corresponds to the length scale of the medium range order in glasses [26-29]. Slack [30] argued that the phonon mean free path cannot be shorter than its wavelength; otherwise the concept of coherent wave-like excitations loses its significance, and a more appropriate picture of heat transport would be that of the random walk. Thus, it is suggested that the plateau separates two regimes, the low temperature (LT) transport by low frequency propagating phonons and the high temperature (HT) transport by high frequency non-propagating thermal vibrations [31-33]. At the frequency of IR crossover, density of states (DOS) in excess to the acoustic phonon (Debye) contribution is observed which accounts for the boson peak in  $c_p/T^3$  [34].

The inset of Fig. 1 shows  $l_{mfp}$  and  $\lambda_c$  in HC, calculated according to [35]:

$$\kappa = \frac{1}{3} c_p \cdot \rho \cdot l_{mfp} \cdot v_a \quad \lambda_c = \frac{v_a}{\nu_c}; \quad h \nu_c \approx 3.8 k_B T \quad (1)$$

using measured temperature dependence of  $\kappa$  and  $c_p$  [15] with  $\rho=1900 \text{ kg/m}^3$  [10] and  $v_a=5900 \text{ m/s}$  [16].

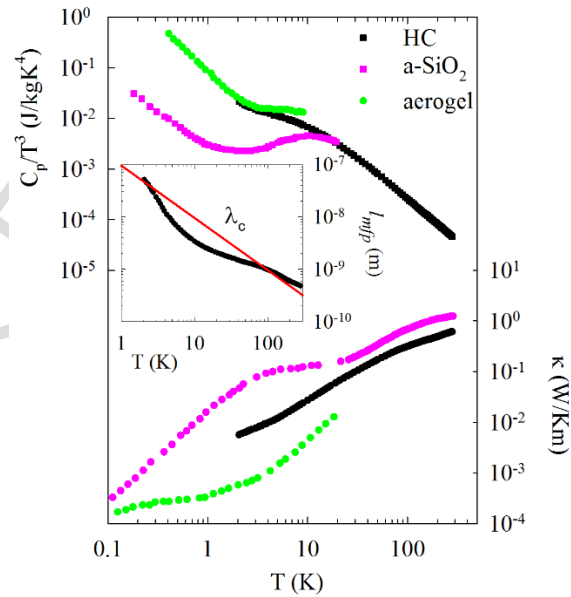


**Fig. 1 - Heat capacity  $c_p$  and thermal conductivity  $\kappa$  of HC [15], a-SiO<sub>2</sub> [17, 18] and SiO<sub>2</sub> aerogel [19]. In the inset is the mean free path  $l_{mfp}$  of HC compared to the wave length of the dominant thermal phonon  $\lambda_c$  (Eq. 1).**

It turns out that  $l_{mfp} < \lambda_c$  in almost entire temperature range, suggesting that  $\kappa$  of HC is in the HT transport regime down to the lowest temperatures. The length scale at IR crossover is  $\sim 100$  nm, much longer than in glasses. However, it is comparable to the correlation length of the fractal structure [36] in aerogels, which is also responsible for IR crossover [37].

The random, fractal-like force-constant structure [31] is also postulated in the “fracton” theory of thermal conductivity in the HT transport regime [38]. We have thus proposed HC as a representative of a new class of *dense fractal systems* [15] since the fractal nature of aerogels is closely related to their extremely low density. The similarity of thermal properties of HC with aerogels, however, raises the question if there is an underlying similarity in the morphology.

We present in this paper the results of an extensive investigation of HC morphology at different length scales, using scanning tunneling microscopy (STM), scanning electron microscopy (SEM), atomic force microscopy (AFM) and scanning acoustic microscopy (SAM). In addition, we have measured Raman spectra and ultrasonic sound attenuation which give complementary information on the size of phonon scatterers. Our results reveal self-similar grain structure at all accessible length scales, making HC an example of dense fractal clustering covering more than six orders of magnitude.

## 2. Experimental procedure

### 2.1. Synthesis and sample preparation

A bulk sample of hard fullerene-based carbon we have used in our measurements was prepared using procedure described in Ref. [10]. Pure C<sub>60</sub> was separated chromatographically from the toluene extract of the carbon soot produced by d.c. arc discharge of graphite rods under a He atmosphere [39, 40]. It showed no electron spin resonance signal at room temperature [40]. The powder was thoroughly ground in a mortar. No attempt was made to estimate or measure particle-size distribution. Pressed pellets 4 mm in diameter and 3 mm in length were sealed in Al<sub>2</sub>O<sub>3</sub> capsules for the high-pressure synthesis in the belt-type apparatus. The pressure was first

raised to 2.6–3 GPa and then the temperature was increased to 700 °C. After 2 hours at 700 °C the temperature was rapidly decreased and finally the pressure was released.

The density of obtained pellets is about 1.9 g/cm<sup>3</sup>, slightly higher than the density of initial C<sub>60</sub> (1.7 g/cm<sup>3</sup>), but lower than the density of graphite (2.1-2.2 g/cm<sup>3</sup>) and much lower than the density of diamond (3.5 g/cm<sup>3</sup>).

The same sample used previously for the thermodynamic investigation [15], in the form of half-disc (diameter~3 mm, thickness~1 mm), was used for all investigations presented in this work. The sample surface was polished with abrasive diamond paste following the procedure suitable for SEM imaging.

## 2.2. *Ultrasonic measurements: scanning acoustic microscopy and sound attenuation*

Spatially resolved image of the elastic properties of the sample has been obtained by scanning acoustic microscopy (SAM) [41]. In the pulse–echo mode or c-scan mode, SAM sends a focused acoustic beam over the sample surface and measures the intensity of reflected subsurface echo. A commercial SAM (HC 1000 Sonix) equipped with ultrasonic pulse generator and a broad band transducer (center frequency of 75 MHz) was used in this study. The half aperture of the acoustic lens was 14° with a working distance of 12 mm. The calculated lateral resolution of the system was about 100 μm in water.

Ultrasonic attenuation  $\alpha$  has been measured at the room temperature in the frequency range 10-150 MHz using Panametrics transducers. Longitudinal sound waves have been generated perpendicular to the parallel flat surfaces, i.e. along the smallest dimension of the sample, the same geometry used previously for the measurement of the temperature dependence of the relative change of the longitudinal sound velocity [15].

## 2.3. *Optical microscopy*

The optical imaging of the sample surface has been performed with Leica Metallux 3 microscope in the reflection mode under built-in light source at different magnifications from ×200 to ×2500. Pictures have been taken with 2048×1536 pixel digital camera.

#### 2.4. *Scanning electron microscopy*

SEM imaging was performed using field emission SEM JSM 7000F at 5 kV at several positions on the sample and at several magnification levels from  $\times 3,300$  to  $\times 100,000$ .

#### 2.5. *Atomic force microscopy*

We have used Multimode Scanning Probe Microscope with Nanoscope IIIa controller (Bruker) with a vertical engagement (JV) 125  $\mu\text{m}$  scanner to perform AFM imaging in contact mode with silicon-nitride probes (NP, Bruker, nom. freq. 56 KHz, nom. spring constant of 0.32 N/m). The nominal tip radius is 20 nm. Measurements were performed in the air ambient temperature and humidity. The linear scanning rate was optimized between 1.5 and 2 Hz with scan resolution of 512 samples per line. Processing and analysis of images were carried out using Nanotec WSxM free software [42]. All images presented are raw data except for the first order two-dimensional flattening.

#### 2.6. *Scanning tunneling microscopy*

STM measurements were performed on Aarhus variable temperature STM (Specs). The data were collected at room temperature in ultra-high vacuum conditions with a base pressure of  $1 \times 10^{-7}$  Pa. The STM tip was grounded and the bias voltage of 128mV was applied to the sample. The data were taken in constant current (topography) mode with the tunneling current of 0.29 nA. STM image analysis was performed in the WSxM software [42].

#### 2.7. *Raman*

The Raman spectra were taken with a HORIBA Jobin Yvon T64000 Raman spectrometer using a triple monochromator. The 514.5 nm line of an Argon laser was used for the excitation.

### 3. **Results**

### 3.1. Imaging on various scales

The imaging techniques we have used in this investigation cover almost continuously a very wide range of length scales from angstroms up to millimeters. These techniques are sensitive to different material properties and widely different sample depths, e.g. from entire cross-section (SEM) to strictly surface elevation (AFM). Although different observed morphologies do not necessarily correlate, they can still provide some insight in the (in)homogeneity of the HC sample.

#### 3.1.1. Scanning acoustic microscopy

Fig. 2 shows typical c-scan SAM image of the sample, which had form of half disk of 3 mm in diameter. The ultrasound amplitude of the reflected subsurface echo was mapped onto 256 color levels so that the color coding bears information on the distribution of local acoustic properties. The contrast of the image was enhanced by histogram equalization.

The acoustic image reveals distinct granularity. The grains tend to cluster so that the areas with strong acoustic contrast are quite well separated. It indicates substantial inhomogeneity in the mechanical properties of the sample. As its  $3 \times 2 \text{ mm}^2$  area corresponds to  $731 \times 430$  pixels, the “grain” diameter in the sample ranges from 1 mm down to  $20 \mu\text{m}$ , which is beyond the actual resolution of  $100 \mu\text{m}$ .

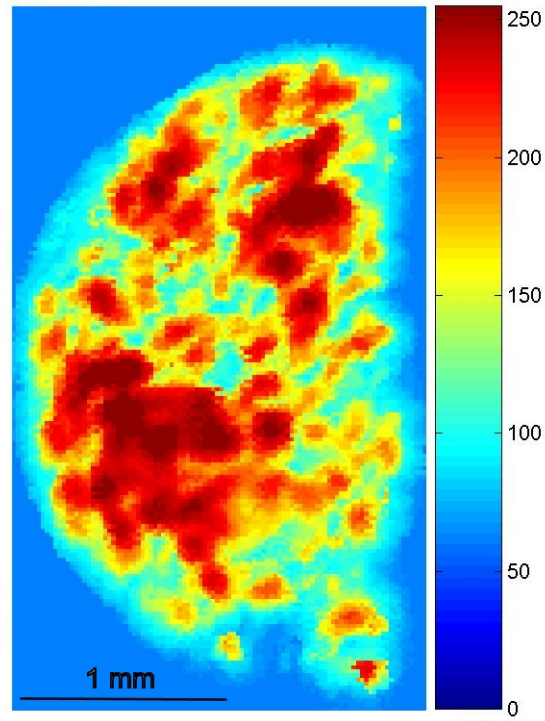


**Fig. 2 - C-scan image (170x100 pixels) acquired at 75 MHz. The ultrasound amplitude of the reflected echo was mapped onto 256 color levels.**

### *3.1.2. Optical microscopy*

Two optical images, taken at  $\times 200$  and  $\times 2500$  magnification, are presented in Fig. 3. The color palette has been converted to 8-bit grayscale. Corresponding areas are  $1.3 \times 1 \text{ mm}^2$  and  $0.1 \times 0.08 \text{ mm}^2$ .

The brighter spots image cannot be seen using diffuse illumination, suggesting that it originates from surface corrugation and not from the variation of HC reflectivity. On low magnification image larger spots are inhomogeneously distributed (similarly as in the SAM images shown in Fig. 2), with the largest size around  $100 \mu\text{m}$ . On high magnification image bright areas are more homogeneously distributed, with uniform brightness spots few  $\mu\text{m}$  in diameter. Blurred parts of the image point to substantial corrugation on longer length scales.

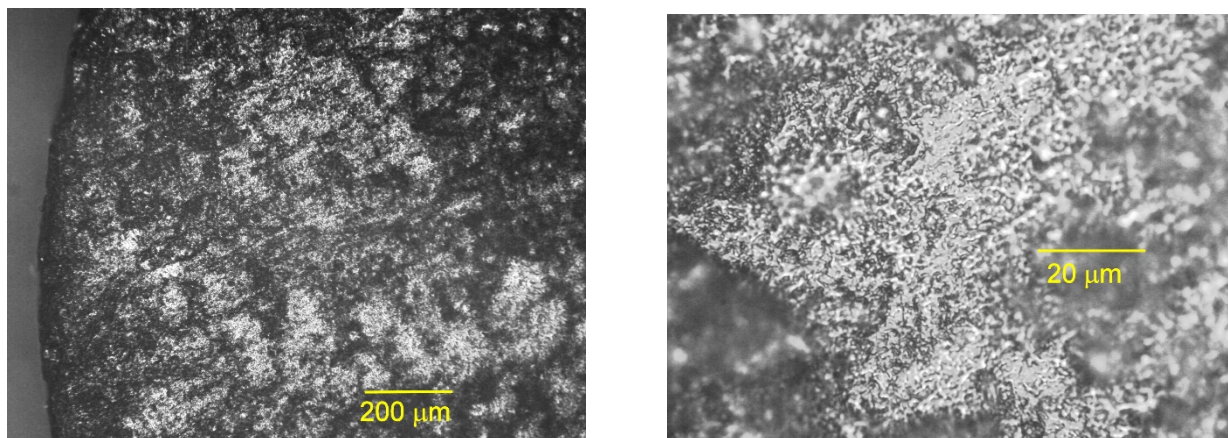


**Fig. 3 - Optical images of HC sample surface,  $1.3 \times 1 \text{ mm}^2$  area taken at  $\times 200$  (left) and  $0.1 \times 0.08 \text{ mm}^2$  area taken at  $\times 2500$  magnification (right). Scaling is presented by yellow line.**

### 3.1.3. Scanning electron microscopy

Two SEM images, taken at  $\times 10^4$  and  $\times 10^5$  magnification, with corresponding areas  $12 \times 9 \text{ }\mu\text{m}^2$  and  $1.2 \times 0.9 \text{ }\mu\text{m}^2$ , are shown in Fig. 4. As the distinction between the “grains” and the “background” in the original image is rather low, we have applied the unsharp mask filter to emphasize the grain edges. The granular structure is present at both magnifications, with size of few 100 nm at lower magnification and few 10 nm at higher magnification.

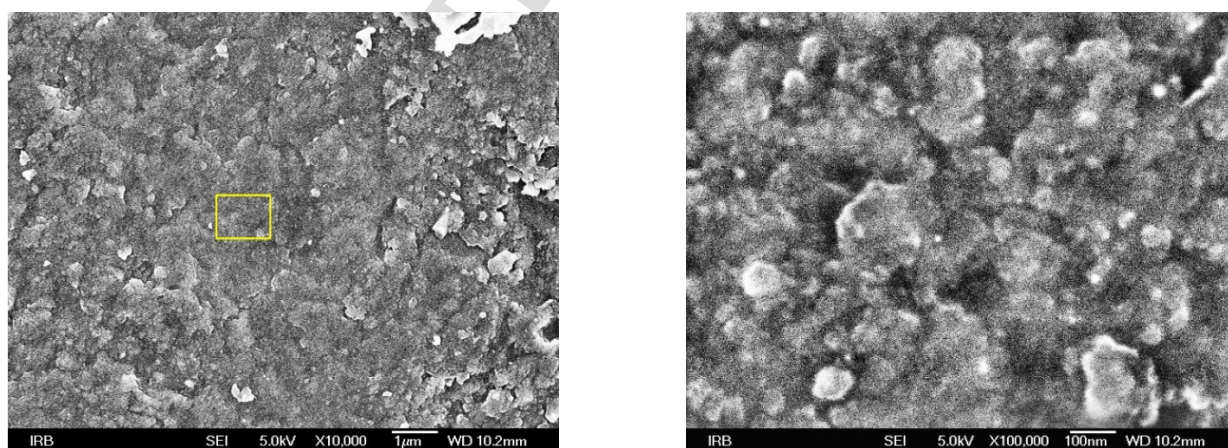


**Fig. 4 - SEM image of the HC sample surface,  $12 \times 9 \text{ }\mu\text{m}^2$  area taken at  $\times 10^4$  (left) and  $1.2 \times 0.9 \text{ }\mu\text{m}^2$  area taken at  $\times 10^5$  magnification (right). Appropriate length scales are presented by white lines and corresponding**

dimensions on the lower right edge. The yellow frame in the left image represents the area presented in the right image.

### 3.1.4. Atomic force microscopy

The surface of HC disc was scanned on several places, on areas ranging from  $0.5 \times 0.5 \mu\text{m}^2$  to  $10 \times 10 \mu\text{m}^2$ . Fig. 5 shows one typical scan and two height profiles along indicated directions. The image covers  $3 \times 3 \mu\text{m}^2$  area, with pixel size  $\approx 6 \times 6 \text{ nm}^2$ , and the height scale is from 0 to 256 nm. The AFM images show inhomogeneous, granular morphology of HC sample, with smaller grains clustering to larger structures. The height profiles indicate that the grain sizes range from 100 nm up to 2  $\mu\text{m}$ .

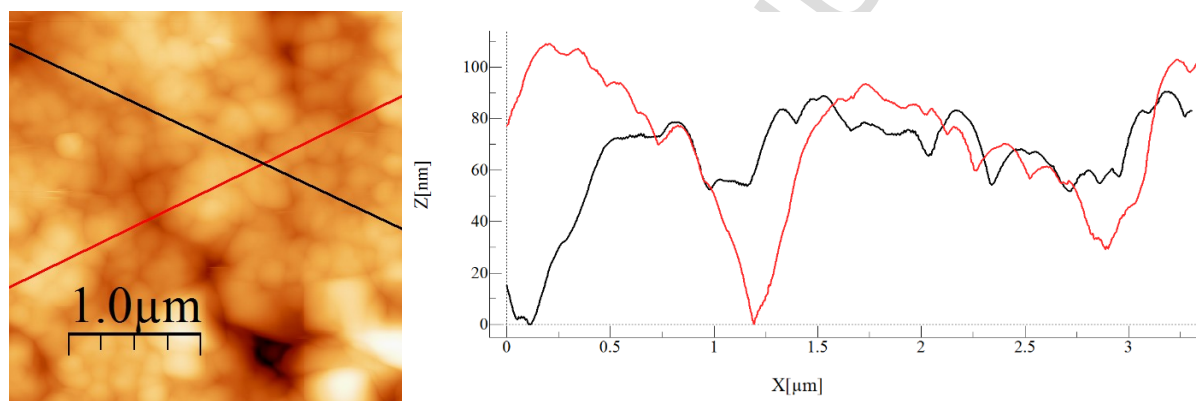


**Fig. 5** - AFM image of  $3 \times 3 \mu\text{m}^2$  HC surface (left) with indicated directions of height profiles (right).

### 3.1.5. STM

STM images were recorded on several places on the sample, across areas ranging from  $3 \times 3 \text{ nm}^2$  to  $20 \times 20 \text{ nm}^2$ . Fig. 6a shows a characteristic STM image of a sample with a blue line denoting a position of the profile in Fig. 6b. On this scale single atoms are observable. The structure appears amorphous, i.e., with atom ordering no longer than few unit cells [43]. Short range atom arrangement, as shown in the inset of Fig. 6a, is characterized by quite large unit cell deviations, ranging between 2.2 Å and 2.8 Å.

The grain width distribution of the observed grains, acquired from the profile analysis of the measured STM images, is presented in Fig. 6c. The distribution shows mean width of  $(2.3 \pm 0.9)$  nm.

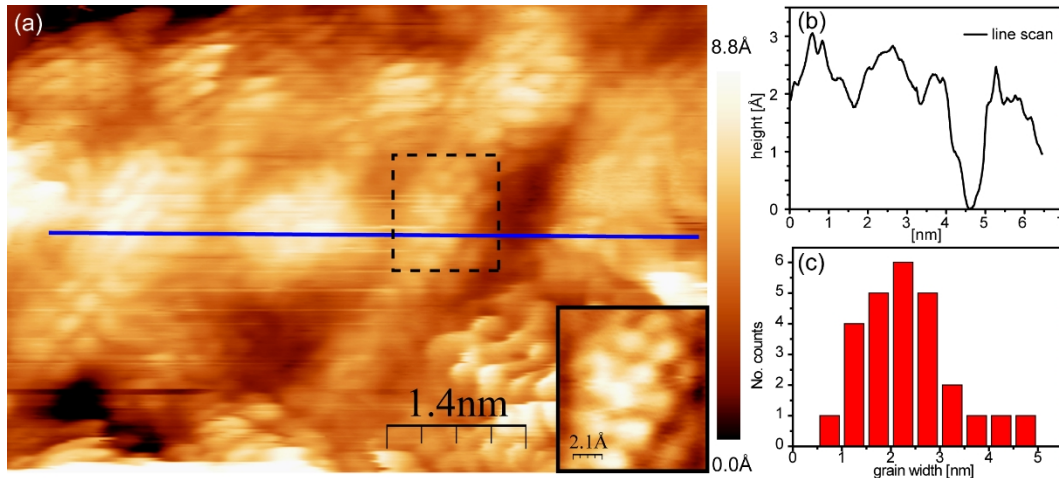


**Fig. 6 - (a) STM image of the HC sample surface. The dashed frame is enlarged in the inset. (b) Height profile along the blue line in (a). (c) Grain width distribution from profiles such as in (b).**

### 3.2. Fractal “clusters of clusters”

The images of HC sample presented in previous sections are obtained by techniques that probe different properties of the sample at different spatial scales. However, they all reveal quite clearly a granular morphology with a wide distribution of grain sizes. At each magnification (or spatial scale), these distributions seem to be bound only by the resolution and the image size, indicating a self-similar morphology in very wide grain size span. It would imply that HC is heterogeneous at all length scales from the size of a single atom to the size of the sample.

In order to obtain more information about the morphology of HC we have tried to quantify systematically the grain size distribution over all available scales. Only in the AFM images the pixel intensity corresponds to the surface height, which would permit the estimation of the grain volume. We have therefore restricted the analysis to the grain area projected to the image plane based on the spatial variation of the intensity.

We have applied several standard image segmentation algorithms used to determine the distinctive objects in the image [44]. However, it turned out that the simpler algorithms cannot

capture the hierarchical “grains within the grains” morphology present in all images, but particularly exemplified in AFM height profiles, Fig. 5. Instead of probing through numerous variations and extensions of increasing mathematical and computational complexity, we have developed another simple algorithm suitable particularly for the samples of such unusual morphology. Grains detected by various image segmentation algorithms in SAM, AFM and STM images corresponded well to the grains determined visually. However, this correspondence was not achieved for optical and SEM images, so we do not report these results.

As an example, we present in Fig. 7 the results of image segmentation for several algorithms on selected AFM image. In Fig. 7a – 7c the original AFM image, covering  $3 \times 3 \mu\text{m}^2$  area with  $512 \times 512$  pixels resolution, is rendered in false colors representing the 256 height levels from blue (lowest) to red (highest) and the lines represent the boundaries of grains determined by different algorithms. The cumulative grain area distribution obtained by different segmentation algorithms is presented in Fig. 7d.

### 3.2.1. Grain determination using standard image segmentation algorithms

The boundaries of the grains obtained by thresholding algorithms [45], which are used for the binary separation of objects from the background in the image, are presented by lines in Fig. 7a. Blue lines are boundaries obtained using the global intensity threshold for the entire image calculated by the Otsu method [46]. The global threshold does not seem appropriate for grain determination on such corrugated surface as in HC, as it misses the majority of smaller grains.

The black lines are the boundaries of the grains obtained by locally adaptive thresholding [45]. This algorithm essentially filters out the slowly varying components of the image, typically the mean intensity within the surrounding window, however with numerous variations and refinements [47]. We have used the Sauvola method [48] with suggested 15 pixels window size and standard deviation bias  $k=0.5$ . Evidently, this algorithm captures smaller grains, however at the expense of larger ones. On the other hand, larger grains can still be determined using global thresholding on the slowly varying components of the image.

In Fig. 7b the image segmentation using the watershed algorithm [49] is presented by the watershed lines (black lines), separating the objects, superimposed on the AFM image. The watershed algorithm collects all pixels from which the intensity strictly increases towards the same

local maximum in one object, i.e. a grain. Unlike the thresholding algorithms, the watershed algorithm “covers” the entire image with grains, including the areas far away and below the particular maximum, which makes the grains larger. We have partially resolved this problem by defining the intensity threshold below which the pixels are considered as background and not included in determining the grain structure. On the other hand, similarly to the local thresholding algorithms, watershed algorithm does not detect larger grains. The waterfalls algorithm [50] can be subsequently applied to merge adjacent grains.

**Fig. 7 – Comparison of several image segmentation algorithms applied to determine the grain area distribution. AFM image of the  $3 \times 3 \mu\text{m}^2$  HC sample surface height, rendered in false colors from lowest (blue) to highest (red), is superimposed in (a) with the grain boundaries obtained by global (blue lines) and local (black lines) thresholding algorithm, in (b) with the grain boundaries obtained by watershed algorithm (black lines) and in (c) with the grain boundaries obtained by hierarchical algorithm (black lines). (d) Cumulative distribution function  $F_p$  (see text) obtained by different image segmentation algorithms presented in Fig. 7a-7c. Dashed lines represent the exponential dependence of  $F_p$  obtained by local thresholding and watershed. Solid line represents the power law dependence with exponent -1. Thin vertical line represents actual AFM resolution.**

### 3.2.2. Hierarchical algorithm for grain determination

Our algorithm, conveniently named “*hierarchical*”, is inspired by contour plots in which a larger closed contour line, representing a large “grain”, can envelope several smaller closed contour lines representing smaller “grains”. The algorithm determines the objects by thresholding at each intensity level. Starting from the highest level (in terms of color coding), it recognizes objects with closed contour lines as grains, tracks their sizes while decreasing the level, and registers grain merging similarly to the cell development tracking in time-lapse microscopy [51]. We have established a hierarchy of grains corresponding to the number of previous merging events. It allows the resolution of merging events, when the grain obtained at lower threshold envelopes several grains at higher threshold. We have set the criterion that the grain stops growing when it is merged with another grain of equal or higher hierarchical level. Unless there is a single highest hierarchical level grain in the merging event, a new grain with a higher hierarchical level is created.

The grain boundaries obtained by hierarchical algorithm are presented by lines in Fig. 7c. The grains touching the image edges, and presumably extending beyond them, are not considered. The grains obtained by hierarchical and thresholding algorithms are similar, however, we do not have to introduce a particular scale, such as averaging window size, to distinguish between smaller and larger grains, i.e. finer and coarser morphology. Also, our algorithm captures naturally the hierarchical structure of smaller grains clustering into larger grains that we would like to describe.

### 3.2.3. Cumulative distribution of grain area sizes

For each algorithm we have collected the two dimensional area sizes  $P$  of individual grains, expressed in the number of pixels, which are then used to construct the empirical cumulative distribution function [52]  $F_P$ , counting the number of grains larger than the  $P$  for every grain.  $F_P$  for all algorithms are presented in Fig. 6d. The nominal AFM tip radius of 20 nm sets the lower limit to the reliability of the grain size evaluation to about 30 pixels, indicated with thin vertical line in Fig. 7d. For comparison between images obtained at different areas actual grain size can be calculated from the number of pixels based on the image area and resolution, and  $F_P$  normalized by the total area of the image, as shown in Fig. 8d.

The algorithms that detect well the smaller grains (local thresholding, watershed, hierarchical) obtain nearly the same number of about 200 grains. The distributions for local thresholding and watershed can be reasonably well approximated with the exponential functions (dashed lines in Fig. 7d), however, with almost one order of magnitude larger mean grain size (750 against 90 pixels) for watershed. For small grain sizes the distribution obtained by hierarchical algorithm is close to the one obtained by local thresholding, however, at larger sizes it approaches the distribution obtained by global thresholding. Its functional dependence is also different and follows roughly the power law with exponent -1 (solid line in Fig. 7d) for almost two orders of magnitude. Combined distribution of area sizes from global and local thresholding (not shown) is actually close to the distribution obtained by hierarchical algorithm. This is not surprising, as the hierarchical algorithm captures naturally both smaller grains and larger grains.

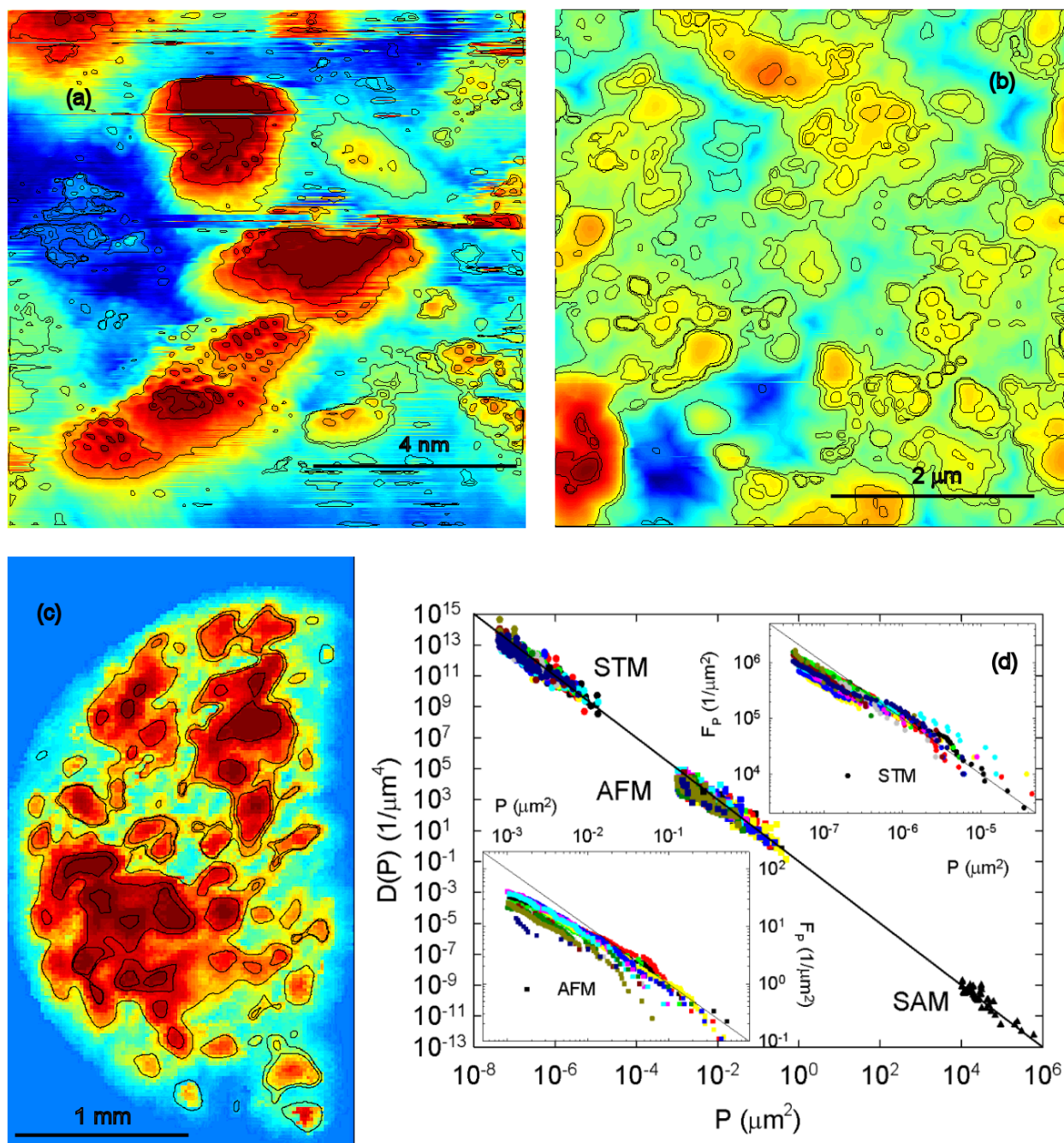


Fig 8 - (a) STM image of the  $10 \times 10 \text{ nm}^2$  HC sample surface (b) AFM image of the  $5 \times 5 \text{ } \mu\text{m}^2$  HC sample surface (c) SAM image of the entire HC sample surface. All images are rendered in false colors from lowest (blue) to highest (red) intensity and superimposed with the grain boundaries obtained by hierarchical algorithm (black lines) (d) Non-cumulative area density function  $D_P$  (see text) obtained by hierarchical algorithm for all STM, AFM and SAM images including those presented in Fig. 8a-8c. Solid line represents the power law dependence with exponent -2. In the insets are the cumulative distribution functions  $F_P$  obtained from AFM and STM

images. Solid lines in the insets represent the power law dependence with exponent -1, same for AFM and STM  $F_p$ .

### 3.2.4. Hierarchical image segmentation of SAM, AFM and STM images

We have applied the hierarchical algorithm to determine the grains and grain area sizes for SAM image and 12 AFM and STM images taken at 3 positions at several different magnifications. The results are presented in Fig. 8. Grain boundaries, represented by lines, are superimposed on the experimental data, rendered in false colors representing the 256 intensity levels from blue (lowest) to red (highest), in Fig. 8a – 8c for selected images. The STM image in Fig. 8a covers  $10 \times 10 \text{ nm}^2$  area and the AFM image in Fig. 8b covers  $5 \times 5 \text{ }\mu\text{m}^2$  area, both with  $512 \times 512$  pixels resolution. The SAM image in Fig. 8c covers  $2 \times 3 \text{ }\mu\text{m}^2$  area with  $430 \times 713$  pixels resolution.  $F_p$  obtained for all AFM and STM images are presented in the insets of Fig. 8d.

### 3.2.5. Power law distribution of grain area sizes

In order to compare the results obtained by different imaging techniques we have calculated the non-cumulative area density function  $D(P)$  as the derivative of  $F_p$  in respect to the grain area [53], as presented in Fig. 8d for all available STM, AFM and SAM images. For each imaging technique a lower cut-off is introduced;  $0.01 \text{ mm}^2$  for SAM according to its lateral resolution,  $10^{-3} \text{ }\mu\text{m}^2$  for AFM, which is approximately the tip area size, and  $4 \text{ \AA}^2$  for STM which is approximately the area of a single carbon atom in Fig. 6.

The lines in Fig. 8a - 8c emphasize very similar hierarchical grain morphology at three very different spatial scales, with smaller grains clustering to form larger ones. Moreover, as presented in Fig. 8d,  $D(P)$  obtained for all STM, AFM and SAM images roughly follows the same power law dependence with exponent -2 over almost 14 orders of magnitude in area size, indicating a scale-free, fractal distribution of grain area sizes [54]. Such a wide range of power law distribution which correspond to length scale variation of almost 7 orders of magnitude, from several  $\text{\AA}$  to 1 mm, is quite exceptional [52].

### 3.3 Elastic mean free path: sound attenuation

The ultrasonic attenuation  $\alpha$  has been measured in the frequency ( $F$ ) range 10 – 150 MHz. In Fig. 9 we present the frequency dependence of the attenuation multiplied by the corresponding wavelength  $\lambda = v_a/F$  for HC sample and for the silica filled epoxy [55] as a reference, where  $v_a = 5900$  m/s for HC [16] and  $v_a = 4200$  m/s for epoxy [55]. The silica inclusions in the epoxy matrix vary in size between 1 and 100  $\mu\text{m}$ .

The dominant contribution to the attenuation of ultrasound in polycrystalline materials comes from the scattering by grains [56, 57].  $\alpha$  typically shows a power law  $F$  dependence with the exponent governed by the ratio of the wavelength  $\lambda$  and the grain diameter  $d$ . At low frequencies, where  $\lambda \gg d$ ,  $\alpha$  is proportional to  $F^4$  due to the Rayleigh (point) scattering, unless it is obscured by the viscoelastic absorption. In the intermediate range where  $\lambda \geq d$ , stochastic scattering with quadratic  $\alpha \sim F^2$  dependence dominates, until  $\alpha$  becomes constant for  $\lambda < d$  in the geometrical regime [58].

As ultrasonic attenuation is inversely proportional to the mean free path,  $\alpha = 1/l_{mfp}$ , the limit where  $\alpha \cdot \lambda \approx 1$  corresponds to the Ioffe-Regel criterion for localization of vibrations and defines the mobility edge for sound waves. By extrapolating the power law dependence of  $\alpha \cdot \lambda$ , as shown in Fig. 9, we estimate that the localization occurs above  $F_1^* \approx 300$  MHz in HC sample which is slightly higher than the frequency  $F_2^* \approx 200$  MHz obtained for epoxy loaded with silica fillers. The corresponding wavelength, i.e. the localization length is  $\approx 20$   $\mu\text{m}$  for both HC and epoxy. In filled epoxy the localization length corresponds to the size of silica inclusions and the strong scattering is attributed to the localization of vibrations within silica grains. By comparison, we can suggest similar grain-like structure at  $\mu\text{m}$  length scales in HC.

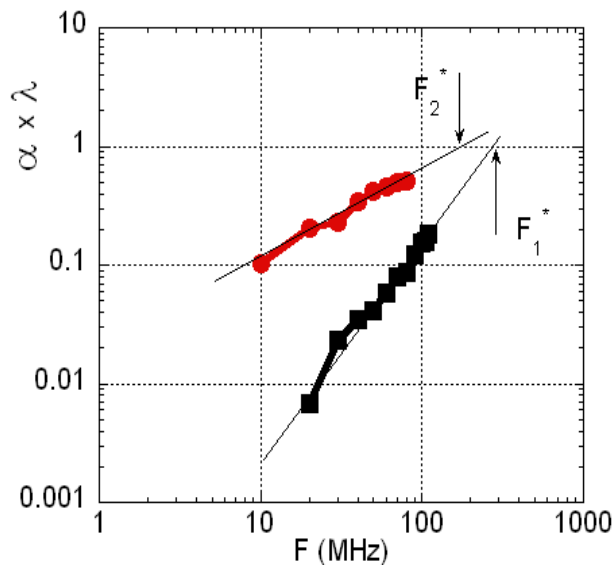


**Fig. 9 - Frequency dependence of the product  $\alpha\lambda$ ,  $\alpha$  being ultrasonic attenuation of longitudinal acoustic waves (or inverse to the elastic mean free path  $\alpha \sim l_{\text{mfp}}^{-1}$ ) and  $\lambda$  being the ultrasonic wave length: hard carbon (black squares) and epoxy matrix (red circles) loaded with micrometer size silica inclusions (1–100  $\mu\text{m}$ ). Extrapolation of power law dependence (solid line) to the crossover frequencies  $F_1^*$  and  $F_2^*$  corresponding to the localization of acoustic wave according to the Ioffe-Regel criterion  $l_{\text{mfp}} \sim \lambda$  or  $\alpha\lambda \sim 1$ .**

### 3.4. Raman

The Raman spectrum of HC sample is shown in Fig. 10. The D and G bands at about 1353  $\text{cm}^{-1}$  and 1590  $\text{cm}^{-1}$  are clearly visible. The intensity ratio of these two bands  $I_D/I_G$  can be used to determine the size of the graphitic crystallites  $L$  in the sample. It has been shown [59-61] that the  $I_D/I_G$  ratio increases with  $L^2$  for  $L < 2$  nm, reaches a maximum of about 2.5 at  $L = 2$  nm and then decreases with  $L^{-1}$  for  $L > 2$  nm. The ratio  $I_D/I_G$ , which in our case is about 0.95, could therefore correspond to two different values of particle size: 1.5 nm or 5.5 nm, on opposite sides of the maximum [61]. By comparing our Raman spectra with similar spectra already reported in literature [60], we can see that our spectrum bears much more resemblance to the spectrum of disordered carbon (which would be in agreement with  $L = 1.5$  nm) than with the spectra of ordered carbon (which would correspond to  $L = 5.5$  nm). This can be seen in particular from the widths of the two bands (which are 90  $\text{cm}^{-1}$  and 55  $\text{cm}^{-1}$  for the D and G bands, respectively) which would

have to be much narrower in the  $L=5.5$  nm case. Therefore we conclude that the particle size in the sample is around 1.5 nm.

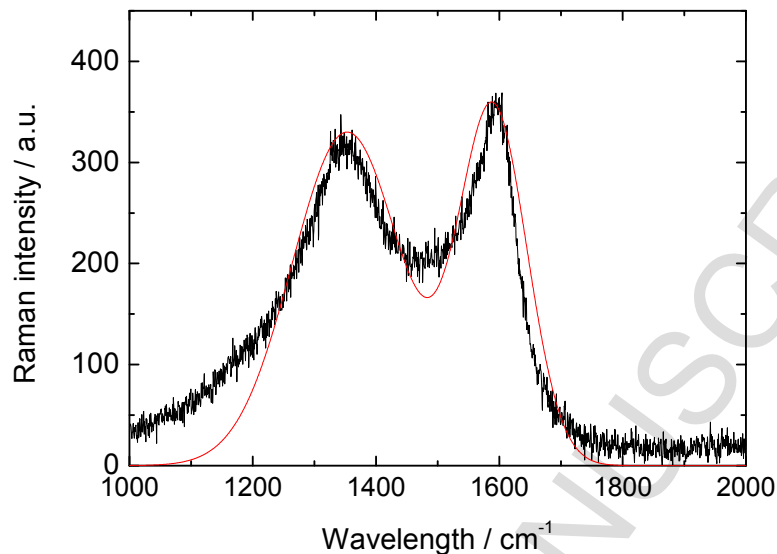


**Fig. 10 - The Raman spectrum of HC sample. The two Gaussians (red line) correspond to the D and G carbon bands.**

#### 4. Discussion

Our extensive investigation of HC morphology at different length scales suggests self-similar grain distribution over length scales covering almost seven orders of magnitude. The structural investigations of HC considered mostly the nanostructure. Previous results on HC samples obtained under comparable conditions point to the disordered  $sp^2$ -type atomic structure with nanocrystals of graphite interlinked by curved molecular fragments [7] or, alternatively, corrugated graphene sheets [62, 63] remaining after the destruction of  $C_{60}$  cages in the parent 2d  $C_{60}$  polymer [6]. Nanocrystalline graphite-like (GL) clusters have been observed by HRTEM with sizes 1.5 – 3 nm [64] or 2 – 4 nm [63] which is consistent with the range of grain sizes observed by STM. The nanocrystallite size estimated from the Raman spectra is on the lower end of this range. On the other hand, SEM images in [16] show microcrystalline grain structure with 8 – 100  $\mu\text{m}$  grain sizes, similar to our SEM results, while at the same spatial scales lamellar structures with 100 nm – 1  $\mu\text{m}$  spacing [16, 64] are observed. However, our AFM data demonstrate that the

grains are continuously present also in the intermediate range between nm (HRTEM) and  $\mu\text{m}$  (SEM) scale, and our SAM data extend the range of grain-like structure to the scales comparable to the sample size. Therefore, the results found in the literature do not contradict ours and all of them added together strongly support our picture of hierarchical grain morphology at all spatial scales.

Persistent heterogeneous morphology over such a wide range is quite unusual. Structural heterogeneity in glasses is revealed only at the level of medium range order of several nm [29]. Distribution of grain sizes in various nano- and poly-crystalline materials usually extends over 1 order of magnitude [65, 66]. Coexisting nano- and micro-scale heterogeneities have been achieved in designed nanostructured thermoelectrics [67]. Only in aggregate nanomaterials [68], such as aerogels, xerogels, pyrogenic silica and carbon, structural data [69] indicate a hierarchy of structural organization, named “multilevel structure” over length scales covering about 5 orders of magnitude from  $\sim\text{nm}$  sized “primary particles” to  $\sim 100\ \mu\text{m}$  sized “agglomerates”. Even in this case, however, self-similar, fractal structure spans at most 2 orders of magnitude between the primary particle size ( $\sim\text{nm}$ ) and the aggregate correlation length ( $\sim 100\ \text{nm}$ ) [70].

Among these aggregates carbon blacks [71] and soots [72], amorphous carbon allotropes obtained in incomplete combustion, show particularly strong similarities with the structure of HC at different spatial scales. Carbon black consists of a fullerene-like globules of concentric graphite nanocrystals [73] which aggregate in larger particles [72, 74, 75]. The graphite nanocrystals are 1-2 nm in size, the globules about 10 – 100 nm and the aggregates can grow beyond  $1\ \mu\text{m}$  [72, 76]. Both STM [77] and AFM [78] images of carbon black are similar with those of HC, with distorted GL domains of several nm and larger particles  $\sim 10 - 100\ \text{nm}$ . It has been also observed [79] that thermally treated carbon black shrinks into a fractal-like domain pattern in the 1 -  $100\ \mu\text{m}$  range, probably due to the release of the heterogeneous stress. Thus a hierarchy of structural organization on very different length scales might not be so uncommon for carbon.

It is tempting to interpret the self-similar fractal-like grain size distribution in HC as a proof that, as in aggregates [80], the HC formation is governed by the same processes at all scales. However, aggregates are obtained by non-equilibrium growth [81] from the dilute, either solvated or gas, phase while HC remains solid under the synthesis conditions [82]. Moreover, considering the entire path of HC formation from initial  $\text{C}_{60}$  powder [83], the heterogeneous structure is formed first at longer scales through the powder compaction [84] at high pressure. As the temperature is

increased, the grains might grow through sintering, but the nucleation and growth of 1D and 2D polymerized  $C_{60}$  phases creates crystallites within the parent  $C_{60}$  crystalline grains [62, 82]. Eventually, at temperatures outside of the region of  $C_{60}$  stability [11], the collapse of molecular cages produces nanocrystalline GL clusters within the parent polymerized phases [63, 64].

The grain size of starting material might have been 10-100  $\mu\text{m}$ , as reported in some investigations [85, 86], which would correspond to the length scales observed in SAM. On the other hand, simple mortar grinding reduces the grain size to 10  $\mu\text{m}$  and below and produces a wide distribution of nanoparticles [87]. Low hardness of pristine  $C_{60}$  [88] makes the powder easily compacted to nominal density already at low pressures [84], however the boundaries between the grains are retained and accumulate stress at higher pressures [84]. Although the sintering is expected to promote the grain growth or coalescence at higher temperatures [89],  $C_{60}$  crystallites do not change the morphology even after  $C_{60}$  cage collapse [90, 91]. The pressure, while promoting compaction, can restrict the grain growth [92]. Thus the wide distribution of grain sizes in HC, particularly at  $\mu\text{m}$  length scales, can come from the particle size distribution in the initial powder.

In the pressure range  $\sim 2\text{-}8$  GPa solid  $C_{60}$  dimerizes, then polymerizes first in 1D chains and then in 2D sheets as the temperature increases [6]. 2D polymerization occurs in  $\{111\}$  dense crystallographic planes containing nearest neighbor  $C_{60}$  molecules in parent f.c.c crystal [62]. The pressure determines the relative abundance of tetragonal and rhombohedral 2D polymer phases [6]. Anisotropic loading, as in belt-type high pressure apparatus, orients the 2D planes parallel to the loading axis [93]. At 3 GPa both phases are present [83, 85, 94] in interpenetrating lamellar domains at 10-100 nm scales which run in two distinct directions [85].

The collapse of  $C_{60}$  cage and the formation of GL phase occurs at same temperatures for  $p\sim 2\text{-}8$  GPa [88], indicating a reconstructive (diffusive) transition [64]. This is corroborated by the slow dynamics of the transition [83]. On the other hand, GL nanocrystals grow along the dense  $C_{60}$  molecular planes of the parent 2D polymer phase and retain their texture [62, 64] indicating displacive (martensitic) transition. Thus the heterogeneity created by intergrowth of polymer phases is preserved in HC [63]. The small size of GL nanocrystals, corresponding to several  $C_{60}$  molecules [83], and their different orientation can be explained by the relaxation of the elastic stress induced by the transformation to GL structure [64].

Theoretical investigations of the structural evolution of  $C_{60}$  crystals at elevated pressures and temperatures are rather sparse and mostly consider the polymorphism and polymerization [96, 97], but only on the level of the unit cell. The pressures at which HC is formed is too low for the amorphisation of  $C_{60}$  crystal obtained in molecular dynamics (MD) simulations [98, 99]. Also, the temperature is too low for the fragmentation of  $C_{60}$  molecule [100]. However, the  $C_{60}$  cage can be broken at much lower temperature through coalescence with other  $C_{60}$  molecules [101-103], driven by the energy gained by the reduction of the local curvature in the system. Simulations show that the first step in the process is necessary the polymerization of  $C_{60}$  molecules [103], as in HC. The final product in the case of isolated dimer is a larger fullerene molecule [104] and in the case of 1D constrained (peapod)  $C_{60}$  chain is a carbon nanotube [102], with distorted metastable intermediate structures [102-104]. It seems natural to suggest that the 2D polymer, from which HC is derived, would coalesce into graphite-like structures. Moreover, the temperature for the peapod coalescence is experimentally determined to be slightly above 1000 K [105], corroborated by MD simulations [102], which is comparable to the temperature of HC formation. The formation of HC from the non-polymerized 3D f.c.c phase [106] results in structure resembling the “crumpled graphene” [107], which can be attributed to the random direction of initial dimerization and later coalescence.

We can conclude that the formation of hierarchical structure of HC is a result of a series of phase transformations, from the crystallization of  $C_{60}$ , over 1D and 2D polymerization to the coalescence of  $C_{60}$  molecules. Except for the crystallization, which determines the initial macroscopic grain structure, each subsequent transformation lowers the symmetry and introduces the textured subdomains in the domain of parent structure, all down to the nanometer level. Such evolution would naturally lead to the hierarchical “grains within the grains” morphology that our results suggests. However, it is not clear if it can explain the self-similar grain size distribution that we have obtained from the analysis.

We expect the heterogeneous morphology over such a wide range of length scales to be responsible for unusual thermal properties of HC. Phenomenologically, this relation is evident from the comparison of thermal properties of nanostructured  $\alpha$ - $SiO_2$  modifications with the increasing length scales of heterogeneity, from densified [112-114], standard [17, 18] and sol-gel [115]  $\alpha$ - $SiO_2$  in the nm range to nanoporous [21] and aerogel [19, 20]  $\alpha$ - $SiO_2$  in the 10 – 100 nm range. As the length scale increases, plateau in  $\kappa$  and boson peak in  $c_p/T^3$  shift towards lower

temperatures, boson peak becomes broader and eventually flattens out and the linear contribution to  $c_p$  increases. We have already noted in the Introduction that the thermal properties of HC are comparable to those of aerogels, in conformation with the heterogeneity in a wide range of length scales. Actually, as these length scales in HC extend to the  $\mu\text{m}$  range and beyond, there should be no plateau down to very low temperatures. Indeed, measurements performed on another HC sample produced under similar conditions [16] show that  $\kappa$  remains quasi linear down to 0.1 K.

So far there is no theory addressing specifically the thermal properties of materials with hierarchical structure beyond some initial attempts with MD simulations [111, 116]. However, the theoretical modeling of thermal properties of glasses, nanocrystalline and polycrystalline materials considers heterogeneity at different length scales, although in relatively narrow ranges. In following, we review some of these theories and try to extrapolate them to the hierarchical case as in HC.

In polycrystalline materials it is well established that the phonon scattering on grain boundaries strongly reduces  $\kappa$  [117-120], while in nanocrystalline materials it even exceeds the Umklapp scattering rate [121] responsible for characteristic  $\sim 1/T$  decrease of  $\kappa$  in crystals at high temperatures. Thus  $\kappa$  of nanocrystalline phase resembles this of amorphous one for small enough grains [119, 122-124] and even the MD simulations fail to demonstrate noticeable differences [125, 126]. This is consistent with the phenomenological model of nanometer clusters [26] in glasses defined by finite correlation length of density [127] or elastic constant [22] fluctuations. These clusters lead to the strong Rayleigh scattering of phonons responsible for the plateau [22]. The correlation length corresponds to the nm length scale of the medium range order in glasses [27].

Several models have been proposed to account for grain scattering, differing substantially in the way the grains are described [128-130]. Nevertheless, in all these models the scattering rate increases strongly when phonon wavelength  $\lambda$  decreases towards characteristic length  $D$  of the heterogeneity and then keeps a constant value, inversely proportional to  $D$ , for  $\lambda < D$ . Thus, the heterogeneity at different length scales should increase the scattering of phonons of corresponding  $\lambda$  and contribute to the reduction of  $\kappa$ , as it has been demonstrated in designed thermoelectrics [67, 131].

If such approach can be applied to HC with very broad, fractal-like distribution of grain sizes, it would imply strong scattering of phonons at (almost) all  $\lambda$ . Our measurements of

ultrasound attenuation suggest that the phonons become strongly scattered, according to the Ioffe-Regel criterion, already at  $\lambda \approx 20 \mu\text{m}$ . HC should consequently have quite low value of  $\kappa$ , at least in comparison to other carbon allotropes. Indeed,  $\kappa$  of HC at room temperature is in the lower range of  $\kappa$  of amorphous carbons of comparable densities [110] and comparable even to  $\kappa$  of low density carbon foams [132]

The strong scattering of phonons at extended spatial scales can also provide explanation for the absence of the plateau in  $\kappa$  of HC. As we have already mentioned in the Introduction, the plateau in glasses is considered to separate the LT heat transport regime by propagating (weakly scattered) phonons and HT transport regime by non-propagating (strongly scattered) thermal vibrations [31-33]. Experimentally, the Ioffe-Regel crossover between weak and strong scattering in a-SiO<sub>2</sub> occurs at frequencies corresponding to  $\lambda$  of the order of several nanometers [133]. If the strong scattering extends to longer  $\lambda$ , as we suggest for HC, and correspondingly lower frequencies, it would extend the HT regime and move the plateau to lower temperatures. Again, ultrasonic attenuation shows that the in HC phonons become strongly scattered at frequencies  $\sim 300$  MHz which would place the plateau in  $\kappa$  around 20 mK.

The heterogeneous structure does not affect  $c_p$  as strongly as  $\kappa$ . In nanocrystalline materials  $c_p$  is moderately increased in the entire temperature range [134, 135]. This increase can be in the most part explained by the lower density of disordered intergrain phase [136, 137]. However, at low temperatures an additional contribution from a low frequency Einstein mode [138, 139] is observed and attributed to low frequency vibrational modes of grains, so-called surface modes [140, 141]. These localized modes can be observed in Raman spectroscopy of embedded nanocrystals [142, 143], and their frequency is reduced as the nanocrystalline size increases [143]. In the phenomenological cluster model of glasses, the boson peak contribution to vibrational DOS [26] is also attributed to the cluster surface mode and its frequency, which also corresponds to IR cross-over frequency [127], determines the temperature of boson peak in  $c_p$ . Similarly as for  $\kappa$ , there is no difference in  $c_p$  of nanocrystalline and amorphous phase obtained from MD simulations [144].

Within such approach, grains of different sizes and correspondingly different frequencies of surface modes would contribute to  $c_p$  at different temperatures. In HC, with very broad, fractal-like distribution of grain sizes, instead of a well-defined boson peak it would produce a broad, flat contribution in excess to the acoustic Debye contribution. With IR cross-over frequency of 300

MHz the Einstein-like lowest mode contribution would have maximum in  $c_p/T^3$  at 5 mK, far below the measurement range in Figure 1.

Low temperature linear contribution to  $c_p$  is typical for glasses [17] and modeled by so-called two-level states (TLS) [145, 146] in local anharmonic atomic potentials. However, it has been shown [147, 148] that any damped vibration in solid contributes to linear  $c_p$  at very low energies. This contribution is proportional to the damping and inversely proportional to the square of vibration frequency [147]. Thus we can understand why this linear contribution to  $c_p$  in HC, where the phonons are strongly scattered already at quite low frequencies, is so much higher than in glasses.

MD simulations of glasses [32, 149], have shown that the structural heterogeneity in glasses translates to the elastic heterogeneity, as suggested previously [22, 26]. Results based on the harmonic approximation of disordered networks [150], which can be extracted from MD simulations phenomenologically, or constructed by introducing random masses, elastic constants or displacements in the lattice [33], reproduce thermal properties well. The plateau in  $\kappa$  corresponds to the IR crossover between the propagating modes with a well-defined wave vector and strongly broadened, diffusive modes at higher energies [32, 151-153]. The excess of DOS contributing to the boson peak corresponds to the nondispersive transversal vibrations in the diffusive regime [149, 154-156].

Within the disordered elastic network approach it was also considered how the variation of disorder strength affects the thermal properties [33, 153, 155, 157-159]. If we adopt that the fractal-like heterogeneous structure of HC produces similar elastic heterogeneity, than these results may be relevant for HC. Increase of disorder strength, measured as the distribution width of elastic constants [33, 155, 157-159], shifts the IR crossover to lower frequencies [33, 157, 158], consistent with the decrease of the temperature of the plateau [158]. The region of excess DOS widens towards low frequencies [33, 157-159], so not only the boson peak shifts to the lower temperatures, but it also becomes wider [158]. At the critical value of disorder strength where the system becomes mechanically unstable the excess DOS again becomes phonon-like, but with additional contribution in excess to the contribution of acoustic phonons [157]. The thermal properties that HC exhibits correspond exactly to this critical disorder strength limit.

Although some of the models explicitly state that the distribution of elastic properties has no spatial correlations [157, 158], MD simulations of different glass models show characteristic

length scales of elastic heterogeneities which exceed the interatomic one [161-164]. For the model  $\alpha$ -SiO<sub>2</sub> [163] this length scale is associated with the boson peak frequency, which is reminiscent of the phenomenological picture of weakly connected clusters [26]. Unfortunately, similar analysis has not been performed for systems with different degree of heterogeneity [155, 160] to check for the variation of this length scale.

Finally, MD simulations have attributed TLS, responsible for low temperature linear contribution to  $c_p$  in glasses, to the slow reversible local atomic rearrangements [165, 166]. They are very similar to the local plastic rearrangements under stress which are observed in athermal MD simulations [167, 168], as both require low energies for activation. The position of local plastic rearrangement coincides with the low frequency mode quasi-localized in the region of the low local elastic modulus [168]. If this reasoning is correct, the density of low elastic modulus regions, and consequently of TLS, should be very high in the system with very high elastic heterogeneity, which HC seems to be.

## 5. CONCLUSIONS

Using different imaging techniques we have demonstrated the heterogeneous granular morphology of HC at widely different length scales, from the order of individual atoms to the order of the sample size. The hierarchical grain size distribution has been quantified for several imaging techniques using appropriate algorithm and it follows a fractal-like power law dependence over almost 14 orders of magnitude in grain area. We show that the heterogeneous morphology over such a wide range of scales could explain unusual thermal properties of HC, particularly its low thermal conductivity. We suggest that the hierarchical morphology of HC emerges from the symmetry lowering phase transformations of C<sub>60</sub> crystal at elevated pressures and temperatures, which offers an alternative way to the reduction of thermal conductivity in bulk materials.

## ACKNOWLEDGEMENTS

D. Starešinić, I. Šrut Rakić, D. Ristić and M. Ivanda gratefully acknowledge financial support by the Center of Excellence for Advanced Materials and Sensors, Croatia.

## REFERENCES

- [1] Robertson J. Diamond-like amorphous carbon. *Materials Science & Engineering R-Reports*. 2002;37(4-6):129-281. doi:10.1016/s0927-796x(02)00005-0
- [2] Vandevelde TCS, Vandierendonck K, Van Stappen M, Mong WD, Perremans P. Cutting applications of DLC, hard carbon and diamond films. *Surface & Coatings Technology*. 1999;113(1-2):80-5. doi:10.1016/s0257-8972(98)00831-7
- [3] Khadem M, Penkov OV, Pukha VE, Maleyev MV, Kim D-E. Ultra-thin nano-patterned wear-protective diamond-like carbon coatings deposited on glass using a C-60 ion beam. *Carbon*. 2014;80:534-43. doi:10.1016/j.carbon.2014.08.093
- [4] Wang ZM, Zhang J, Han X, Li QF, Wang ZL, Wei R. Corrosion and salt scale resistance of multilayered diamond-like carbon film in CO<sub>2</sub> saturated solutions. *Corrosion Science*. 2014;86:261-7. doi:10.1016/j.corsci.2014.05.015
- [5] Dearnaley G, Arps JH. Biomedical applications of diamond-like carbon (DLC) coatings: A review. *Surface & Coatings Technology*. 2005;200(7):2518-24. doi:10.1016/j.surfcoat.2005.07.077
- [6] Alvarez-Murga M, Hodeau JL. Structural phase transitions of C-60 under high-pressure and high-temperature. *Carbon*. 2015;82:381-407. doi:10.1016/j.carbon.2014.10.083
- [7] Brazhkin VV, Lyapin AG. Hard and superhard carbon phases synthesized from fullerenes under pressure. *Journal of Superhard Materials*. 2012;34(6):400-23. doi:10.3103/s1063457612060135
- [8] Sundqvist B. Fullerenes under high pressures. *Advances in Physics*. 1999;48(1):1-134. doi:10.1080/000187399243464
- [9] Regueiro MN, Monceau P, Hodeau JL. CRUSHING C60 TO DIAMOND AT ROOM-TEMPERATURE. *Nature*. 1992;355(6357):237-9. doi:10.1038/355237a0
- [10] Kozlov ME, Hirabayashi M, Nozaki K, Tokumoto M, Ihara H. TRANSFORMATION OF C-60 FULLERENES INTO A SUPERHARD FORM OF CARBON AT MODERATE PRESSURE. *Applied Physics Letters*. 1995;66(10):1199-201. doi:10.1063/1.113856
- [11] Sundar CS, Bharathi A, Hariharan Y, Janaki J, Sastry VS, Radhakrishnan TS. THERMAL-DECOMPOSITION OF C-60. *Solid State Communications*. 1992;84(8):823-6. doi:10.1016/0038-1098(92)90098-t
- [12] Rau JV, Teghil R, De Bonis A, Generosi A, Paci B, Generosi R, et al. Pulsed laser deposition of hard and superhard carbon thin films from C-60 targets. *Diamond and Related Materials*. 2010;19(1):7-14. doi:10.1016/j.diamond.2009.10.010
- [13] Biljakovic K, Smontara A, Staresinic D, Pajic D, Kozlov ME, Hirabayashi M, et al. Thermal transport in hard carbon prepared from C-60 fullerene. *Journal of Physics-Condensed Matter*. 1996;8(3):L27-L32. doi:10.1088/0953-8984/8/3/001
- [14] Maniwa Y, Sato M, Kume K, Kozlov ME, Tokumoto M. Comparative NMR study of new carbon forms. *Carbon*. 1996;34(10):1287-91. doi:10.1016/0008-6223(96)00116-9
- [15] Biljakovic K, Kozlov M, Staresinic D, Saint-Paul M. The amorphous nature of C-60 hard carbon manifested in its specific heat, sound velocity and heat conduction. *Journal of Physics-Condensed Matter*. 2002;14(25):6403-12. doi:10.1088/0953-8984/14/25/309
- [16] Lasjaunias JC, Saint-Paul M, Bilusic A, Smontara A, Gradecak S, Tonejc AM, et al. Acoustic and thermal transport properties of hard carbon formed from C-60 fullerene. *Physical Review B*. 2002;66(1). doi:10.1103/PhysRevB.66.014302
- [17] Zeller RC, Pohl RO. THERMAL CONDUCTIVITY AND SPECIFIC HEAT OF NONCRYSTALLINE SOLIDS. *Physical Review B*. 1971;4(6):2029-&. doi:10.1103/PhysRevB.4.2029
- [18] Cahill DG, Pohl RO. THERMAL-CONDUCTIVITY OF AMORPHOUS SOLIDS ABOVE THE PLATEAU. *Physical Review B*. 1987;35(8):4067-73. doi:10.1103/PhysRevB.35.4067
- [19] Degoer AM, Calemczuk R, Salce B, Bon J, Bonjour E, Maynard R. LOW-TEMPERATURE ENERGY EXCITATIONS AND THERMAL-PROPERTIES OF SILICA AEROGELS. *Physical Review B*. 1989;40(12):8327-35. doi:10.1103/PhysRevB.40.8327

- [20] Bernasconi A, Sleator T, Posselt D, Kjems JK, Ott HR. DYNAMIC PROPERTIES OF SILICA AEROGELS AS DEDUCED FROM SPECIFIC-HEAT AND THERMAL-CONDUCTIVITY MEASUREMENTS. *Physical Review B*. 1992;45(18):10363-76. doi:10.1103/PhysRevB.45.10363
- [21] Watson SK, Pohl RO. Low-energy lattice vibrations of porous silica glass. *Physical Review B*. 2003;68(10). doi:10.1103/PhysRevB.68.104203
- [22] Graebner JE, Golding B, Allen LC. PHONON LOCALIZATION IN GLASSES. *Physical Review B*. 1986;34(8):5696-701. doi:10.1103/PhysRevB.34.5696
- [23] Kittel C. Interpretation of the Thermal Conductivity of Glasses. *Physical Review*. 1949;75(6):972-4. doi:10.1103/PhysRev.75.972
- [24] Ziman JM. *Electrons and phonons*. Oxford: Clarendon Press; 1960.
- [25] Narayanamurti V, Pohl RO. Tunneling states of defects in solids. *Reviews of Modern Physics*. 1970;42(2):201-36. doi:10.1103/RevModPhys.42.201
- [26] Duval E, Boukenter A, Achibat T. VIBRATIONAL DYNAMICS AND THE STRUCTURE OF GLASSES. *Journal of Physics-Condensed Matter*. 1990;2(51):10227-34. doi:10.1088/0953-8984/2/51/001
- [27] Elliott SR. MEDIUM-RANGE STRUCTURAL ORDER IN COVALENT AMORPHOUS SOLIDS. *Nature*. 1991;354(6353):445-52. doi:10.1038/354445a0
- [28] Sokolov AP, Kisliuk A, Soltwisch M, Quitmann D. MEDIUM-RANGE ORDER IN GLASSES - COMPARISON OF RAMAN AND DIFFRACTION MEASUREMENTS. *Physical Review Letters*. 1992;69(10):1540-3. doi:10.1103/PhysRevLett.69.1540
- [29] Baldi G, Zanatta M, Gilioli E, Milman V, Refson K, Wehinger B, et al. Emergence of Crystal-like Atomic Dynamics in Glasses at the Nanometer Scale. *Physical Review Letters*. 2013;110(18). doi:10.1103/PhysRevLett.110.185503
- [30] Slack GA. The Thermal Conductivity of Nonmetallic Crystals. In: Ehrenreich H, Seitz F, Turnbull D, eds. *Solid State Physics Advances in Research and Applications*.34. New York: Academic Press, INC. 1979, p. 1-73. isbn:0-12-607734-7
- [31] Alexander S, Laermans C, Orbach R, Rosenberg HM. FRACTION INTERPRETATION OF VIBRATIONAL PROPERTIES OF CROSS-LINKED POLYMERS, GLASSES, AND IRRADIATED QUARTZ. *Physical Review B*. 1983;28(8):4615-9. doi:10.1103/PhysRevB.28.4615
- [32] Feldman JL, Kluge MD, Allen PB, Wooten F. THERMAL-CONDUCTIVITY AND LOCALIZATION IN GLASSES - NUMERICAL STUDY OF A MODEL OF AMORPHOUS-SILICON. *Physical Review B*. 1993;48(17):12589-602. doi:10.1103/PhysRevB.48.12589
- [33] Schirmacher W, Diezemann G, Ganter C. Harmonic vibrational excitations in disordered solids and the "boson peak". *Physical Review Letters*. 1998;81(1):136-9. doi:10.1103/PhysRevLett.81.136
- [34] Buchenau U, Prager M, Nucker N, Dianoux AJ, Ahmad N, Phillips WA. LOW-FREQUENCY MODES IN VITREOUS SILICA. *Physical Review B*. 1986;34(8):5665-73. doi:10.1103/PhysRevB.34.5665
- [35] Klitsner T, Pohl RO. PHONON-SCATTERING AT SILICON CRYSTAL-SURFACES. *Physical Review B*. 1987;36(12):6551-65. doi:10.1103/PhysRevB.36.6551
- [36] Vacher R, Courtens E, Coddens G, Heidemann A, Tsujimi Y, Pelous J, et al. CROSSOVERS IN THE DENSITY OF STATES OF FRACTAL SILICA AEROGELS. *Physical Review Letters*. 1990;65(8):1008-11. doi:10.1103/PhysRevLett.65.1008
- [37] Courtens E, Pelous J, Phalippou J, Vacher R, Woignier T. BRILLOUIN-SCATTERING MEASUREMENTS OF PHONON-FRACTION CROSSOVER IN SILICA AEROGELS. *Physical Review Letters*. 1987;58(2):128-31. doi:10.1103/PhysRevLett.58.128
- [38] Jagannathan A, Orbach R, Entinwohlman O. THERMAL-CONDUCTIVITY OF AMORPHOUS MATERIALS ABOVE THE PLATEAU. *Physical Review B*. 1989;39(18):13465-77. doi:10.1103/PhysRevB.39.13465
- [39] Scrivens WA, Bedworth PV, Tour JM. PURIFICATION OF GRAM QUANTITIES OF C-60 - A NEW INEXPENSIVE AND FACILE METHOD. *Journal of the American Chemical Society*. 1992;114(20):7917-9. doi:10.1021/ja00046a051
- [40] Tokumoto M, Tanaka Y, Kinoshita N, Kinoshita T, Ishibashi S, Ihara H. CHARACTERIZATION OF SUPERCONDUCTING ALKALI AND ALKALINE-EARTH FULLERIDES PREPARED BY THERMAL-DECOMPOSITION OF AZIDES. *Journal of Physics and Chemistry of Solids*. 1993;54(12):1667-73. doi:10.1016/0022-3697(93)90280-5
- [41] Briggs A. *Acoustic microscopy*. Oxford: Clarendon Press; 1992.

- [42] Horcas I, Fernandez R, Gomez-Rodriguez JM, Colchero J, Gomez-Herrero J, Baro AM. WSXM: A software for scanning probe microscopy and a tool for nanotechnology. *Review of Scientific Instruments*. 2007;78(1). doi:10.1063/1.2432410
- [43] Kayser T, Ostadrahimi AH, Schlenz H, Beck J, Wandelt K. Scanning probe microscopic investigations of amorphous tellurium subhalides. *Journal of Non-Crystalline Solids*. 2005;351(12-13):1097-102. doi:10.1016/j.jnoncrysol.2005.01.023
- [44] Jalba AC, Wilkinson MH, Roerdink J. Automatic segmentation of diatom images for classification. *Microsc Res Tech*. 2004;65(1-2):72-85. doi:10.1002/jemt.20111
- [45] Sezgin M, Sankur B. Survey over image thresholding techniques and quantitative performance evaluation. *Journal of Electronic Imaging*. 2004;13(1):146-68. doi:10.1117/1.16313161
- [46] Otsu N. Threshold selection method from gray-level histograms. *Ieee Transactions on Systems Man and Cybernetics*. 1979;9(1):62-6.
- [47] Gatos B, Pratikakis I, Perantonis SJ. Adaptive degraded document image binarization. *Pattern Recognition*. 2006;39(3):317-27. doi:10.1016/j.patcog.2005.09.010
- [48] Sauvola J, Pietikainen M. Adaptive document image binarization. *Pattern Recognition*. 2000;33(2):225-36. doi:10.1016/s0031-3203(99)00055-2
- [49] Meyer F. TOPOGRAPHIC DISTANCE AND WATERSHED LINES. *Signal Processing*. 1994;38(1):113-25. doi:10.1016/0165-1684(94)90060-4
- [50] Beucher S. Watershed, hierarchical segmentation and waterfall algorithm. In: Serra J, Soille P, eds. *Mathematical Morphology and Its Applications to Image Processing*. Netherlands: Kluwer Academic Publishers 1994, p. 69-76. isbn:978-94-011-1040-2
- [51] Al-Kofahi O, Radke RJ, Goderie SK, Shen Q, Temple S, Roysam B. Automated cell lineage construction - A rapid method to analyze clonal development established with murine neural progenitor cells. *Cell Cycle*. 2006;5(3):327-35. doi:10.4161/cc.5.3.2426
- [52] Newman MEJ. Power laws, Pareto distributions and Zipf's law. *Contemporary Physics*. 2005;46(5):323-51. doi:10.1080/00107510500052444
- [53] Malamud B, Turcotte D. An inverse cascade explanation for the power-law frequency-area statistics of earthquakes, landslides and wildfires. In: Cello G, Malamud B, eds. *Fractal Analysis for Natural Hazards*. London: Geological Society 2006, p. 1-9. isbn:978-1862392014
- [54] Nakayama T, Yakubo K. *Fractal Concepts in Condensed Matter Physics*. Berlin Heidelberg: Springer-Verlag 2003.
- [55] Clement A, Saint-Paul M. Ultrasonic measurements of microelectronic molding compounds. *Journal of Materials Science-Materials in Electronics*. 2002;13(1):21-5. doi:10.1023/a:1013190812644
- [56] Papadakis EP. Physical acoustics and microstructure of iron alloys. *Inter Metals Review*. 1984;29(1):1-24. doi:10.1179/imtr.1984.29.1.1
- [57] Zeng F, Agnew SR, Raesinia B, Myneni GR. Ultrasonic Attenuation Due to Grain Boundary Scattering in Pure Niobium. *Journal of Nondestructive Evaluation*. 2010;29(2):93-103. doi:10.1007/s10921-010-0068-2
- [58] Papadakis E. REVISED GRAIN-SCATTERING FORMULAS AND TABLES. *Journal of the Acoustical Society of America*. 1965;37(4):703-&. doi:10.1121/1.1909399
- [59] Tuinstra F, Koenig JL. RAMAN SPECTRUM OF GRAPHITE. *Journal of Chemical Physics*. 1970;53(3):1126-&. doi:10.1063/1.1674108
- [60] Escribano R, Sloan JJ, Siddique N, Sze N, Dudev T. Raman spectroscopy of carbon-containing particles. *Vibrational Spectroscopy*. 2001;26(2):179-86. doi:10.1016/s0924-2031(01)00106-0
- [61] Ferrari AC, Robertson J. Interpretation of Raman spectra of disordered and amorphous carbon. *Physical Review B*. 2000;61(20):14095-107. doi:10.1103/PhysRevB.61.14095
- [62] Lepoittevin C, Alvarez-Murga M, Marques L, Mezouar M, Hodeau JL. Structural characterization of corrugated anisotropic graphene-based carbons obtained from the collapse of 2D C-60 polymers. *Carbon*. 2013;52:278-87. doi:10.1016/j.carbon.2012.09.029
- [63] Chernogorova O, Potapova I, Drozdova E, Sirotinkin V, Soldatov AV, Vasiliev A, et al. Structure and physical properties of nanoclustered graphene synthesized from C-60 fullerene under high pressure and high temperature. *Applied Physics Letters*. 2014;104(4). doi:10.1063/1.4863470
- [64] Tat'yanin EV, Lyapin AG, Mukhamadiarov VV, Brazhkin VV, Vasiliev AL. Mechanism of formation of the superhard disordered graphite-like phase from fullerite C-60 under pressure. *Journal of Physics-Condensed Matter*. 2005;17(2):249-56. doi:10.1088/0953-8984/17/2/001

- [65] Ungar T, Gubicza J, Ribarik G, Borbely A. Crystallite size distribution and dislocation structure determined by diffraction profile analysis: principles and practical application to cubic and hexagonal crystals. *Journal of Applied Crystallography*. 2001;34:298-310. doi:10.1107/s0021889801003715
- [66] Kim YW, Mitomo M, Hirotsuru H. GRAIN-GROWTH AND FRACTURE-TOUGHNESS OF FINE-GRAINED SILICON-CARBIDE CERAMICS. *Journal of the American Ceramic Society*. 1995;78(11):3145-8. doi:10.1111/j.1151-2916.1995.tb09100.x
- [67] Biswas K, He JQ, Blum ID, Wu CI, Hogan TP, Seidman DN, et al. High-performance bulk thermoelectrics with all-scale hierarchical architectures. *Nature*. 2012;489(7416):414-8. doi:10.1038/nature11439
- [68] Albers P, Maier M, Reisinger M, Hannebauer B, Weinand R. Physical boundaries within aggregates - differences between amorphous, para-crystalline, and crystalline Structures. *Crystal Research and Technology*. 2015;50(11):846-65. doi:10.1002/crat.201500040
- [69] Schaefer DW, Rieker T, Agamalian M, Lin JS, Fischer D, Sukumaran S, et al. Multilevel structure of reinforcing silica and carbon. *Journal of Applied Crystallography*. 2000;33(1):587-91. doi:10.1107/s0021889800001199
- [70] Vacher R, Woignier T, Pelous J, Courtens E. STRUCTURE AND SELF-SIMILARITY OF SILICA AEROGELS. *Physical Review B*. 1988;37(11):6500-3. doi:10.1103/PhysRevB.37.6500
- [71] Donnet JB. 50 YEARS OF RESEARCH AND PROGRESS ON CARBON-BLACK. *Carbon*. 1994;32(7):1305-10. doi:10.1016/0008-6223(94)90116-3
- [72] Clague ADH, Donnet J, Wang TK, Peng JCM. A comparison of diesel engine soot with carbon black. *Carbon*. 1999;37(10):1553-65. doi:10.1016/s0008-6223(99)00035-4
- [73] Heidenreich RD, Hess WM, Ban LL. A TEST OBJECT AND CRITERIA FOR HIGH RESOLUTION ELECTRON MICROSCOPY. *Journal of Applied Crystallography*. 1968;1:1-&. doi:10.1107/s0021889868004930
- [74] Ozawa M, Goto H, Kusunoki M, Osawa E. Continuously growing spiral carbon nanoparticles as the intermediates in the formation of fullerenes and nanonions. *Journal of Physical Chemistry B*. 2002;106(29):7135-8. doi:10.1021/jp025639z
- [75] Du JM, Liu ZM, Li ZH, Han BX, Sun ZY, Huang Y. Carbon onions synthesized via thermal reduction of glycerin with magnesium. *Materials Chemistry and Physics*. 2005;93(1):178-80. doi:10.1016/j.matchemphys.2005.03.012
- [76] Deshmukh AA, Mhlanga SD, Coville NJ. Carbon spheres. *Materials Science & Engineering R-Reports*. 2010;70(1-2):1-28. doi:10.1016/j.mser.2010.06.017
- [77] Donnet JB, Custodero E. ORDERED STRUCTURES OBSERVED BY SCANNING TUNNELING MICROSCOPY AT ATOMIC SCALE ON CARBON-BLACK SURFACES. *Carbon*. 1992;30(5):813-5. doi:10.1016/0008-6223(92)90165-s
- [78] Niedermeier W, Stierstorfer J, Kreitmeier S, Metz O, Goritz D. MORPHOLOGICAL INVESTIGATIONS ON CARBON-BLACK PARTICLES BY ATOMIC-FORCE MICROSCOPY. *Rubber Chemistry and Technology*. 1994;67(1):148-58. doi:10.5254/1.3538661
- [79] Buchholz DB, Doherty SP, Chang RPH. Mechanism for the growth of multiwalled carbon-nanotubes from carbon black. *Carbon*. 2003;41(8):1625-34. doi:10.1016/s0008-6223(03)00110-6
- [80] Nicolas-Carlock JR, Carrillo-Estrada JL, Dossetti V. Fractality a la carte: a general particle aggregation model. *Scientific Reports*. 2016;6. doi:10.1038/srep19505
- [81] Benjacob E, Garik P. THE FORMATION OF PATTERNS IN NONEQUILIBRIUM GROWTH. *Nature*. 1990;343(6258):523-30. doi:10.1038/343523a0
- [82] Alvarez-Murga M, Bleuët P, Marques L, Lepoittevin C, Boudet N, Gabarino G, et al. Microstructural mapping of C60 phase transformation into disordered graphite at high pressure, using X-ray diffraction microtomography. *Journal of Applied Crystallography*. 2011;44:163-71. doi:10.1107/s0021889810050399
- [83] Dzwilewski A, Talyzin A, Bromiley G, Dub S, Dubrovinsky L. Characterization of phases synthesized close to the boundary of C-60 collapse at high temperature high pressure conditions. *Diamond and Related Materials*. 2007;16(8):1550-6. doi:10.1016/j.diamond.2006.12.040
- [84] Kolomiets LL, Solonin SM, Skorokhod VV. Compaction and elastic relaxation of fullerite powder. *Powder Metallurgy and Metal Ceramics*. 1999;38(9-10):488-92.
- [85] Wood RA, Lewis MH, West G, Bennington SM, Cain MG, Kitamura N. Transmission electron microscopy, electron diffraction and hardness studies of high-pressure and high-temperature treated C-60. *Journal of Physics-Condensed Matter*. 2000;12(50):10411-21. doi:10.1088/0953-8984/12/50/304

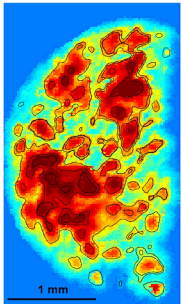
- [86] Brazhkin VV, Lyapin AG, Popova SV, Bayliss SC, Varfolomeeva TD, Voloshin RN, et al. Interplay between the structure and properties of new metastable carbon phases obtained under high pressures from fullerite C-60 and carbyne. *Jetp Letters*. 2002;76(11):681-92. doi:10.1134/1.1545583
- [87] Deguchi S, Mukai S, Yamazaki T, Tsudome M, Horikoshi K. Nanoparticles of Fullerene C-60 from Engineering of Antiquity. *Journal of Physical Chemistry C*. 2010;114(2):849-56. doi:10.1021/jp909331n
- [88] Lyapin AG, Brazhkin VV, Gromnitskaya EL, Popova SV, Stal'gorova OV, Voloshin RN, et al. Hardening of fullerite C60 during temperature-induced polymerization and amorphization under pressure. *Applied Physics Letters*. 2000;76(6):712-4.
- [89] German RM. Sintering simplified: Surface area, density, and grain size relations. *Materials Science Forum* 2016, p. 50-75.
- [90] Leifer SD, Goodwin DG, Anderson MS, Anderson JR. Thermal decomposition of a fullerene mix. *Physical Review B*. 1995;51(15):9973-8. doi:10.1103/PhysRevB.51.9973
- [91] Mochida I, Egashira M, Korai Y, Yokogawa K. Structural changes of fullerene by heat-treatment up to graphitization temperature. *Carbon*. 1997;35(12):1707-12. doi:10.1016/s0008-6223(97)00125-5
- [92] Ji W, Rehman SS, Wang W, Wang H, Wang Y, Zhang J, et al. Sintering boron carbide ceramics without grain growth by plastic deformation as the dominant densification mechanism. *Scientific Reports*. 2015;5. doi:10.1038/srep15827
- [93] Lyapin AG, Mukhamadiarov VV, Brazhkin VV, Popova SV, Kondrin MV, Sadykov RA, et al. Structural and elastic anisotropy of carbon phases prepared from fullerite C-60. *Applied Physics Letters*. 2003;83(19):3903-5. doi:10.1063/1.1625432
- [94] Davydov VA, Kashevarova LS, Rakhmanina AV, Agafonov V, Céolin R, Szwarc H. Structural studies of C60 transformed by temperature and pressure treatments. *Carbon*. 1997;35(6):735-43.
- [95] Meakin P. FRACTAL AGGREGATES. *Advances in Colloid and Interface Science*. 1988;28(4):249-331.
- [96] Volonakis G, Tsetseris L, Logothetidis S. Continuous transformations of C-60 crystals: polymorphs, polymers, and the ideal strength of fullerenes. *Journal of Physics-Condensed Matter*. 2013;25(43):8. doi:10.1088/0953-8984/25/43/435303
- [97] Yamagami Y, Saito S. Polymerized sp(2)-sp(3) hybrid metallic phase of C-60 as obtained via constant-pressure molecular dynamics. *Physical Review B*. 2009;79(4). doi:10.1103/PhysRevB.79.045425
- [98] Zhang BL, Wang CZ, Ho KM, Chan CT. STRUCTURE OF COLLAPSED SOLID C-60. *Europhysics Letters*. 1994;28(4):219-24. doi:10.1209/0295-5075/28/4/001
- [99] Moseler M, Riedel H, Gumbsch P, Staring J, Mehlig B. Understanding of the phase transformation from fullerite to amorphous carbon at the microscopic level. *Physical Review Letters*. 2005;94(16). doi:10.1103/PhysRevLett.94.165503
- [100] Qian DB, Ma X, Chen Z, Zhang DC, Zhang SF, Li B, et al. Determining excitation temperature of fragmented C-60 via momentum distributions of fragments. *Physical Chemistry Chemical Physics*. 2011;13(8):3328-33. doi:10.1039/c0cp00773k
- [101] Xu ZW, Liang ZL, Ding F. Isomerization of sp(2)-hybridized carbon nanomaterials: structural transformation and topological defects of fullerene, carbon nanotube, and graphene. *Wiley Interdisciplinary Reviews-Computational Molecular Science*. 2017;7(2). doi:10.1002/wcms.1283
- [102] Hernandez E, Meunier V, Smith BW, Rurali R, Terrones H, Nardelli MB, et al. Fullerene coalescence in nanopeapods: A path to novel tubular carbon. *Nano Letters*. 2003;3(8):1037-42. doi:10.1021/nl034283f
- [103] Han S, Yoon M, Berber S, Park N, Osawa E, Ihm J, et al. Microscopic mechanism of fullerene fusion. *Physical Review B - Condensed Matter and Materials Physics*. 2004;70(11):113402-1--4. doi:10.1103/PhysRevB.70.113402
- [104] Ding F, Yakobson BI. Energy-Driven Kinetic Monte Carlo Method and Its Application in Fullerene Coalescence. *Journal of Physical Chemistry Letters*. 2014;5(17):2922-6. doi:10.1021/jz501324y
- [105] Smith DS, Fayette S, Grandjean S, Martin C, Telle R, Tonnessen T. Thermal resistance of grain boundaries in alumina ceramics and refractories. *Journal of the American Ceramic Society*. 2003;86(1):105-11.
- [106] Brazhkin VV, Solozhenko VL, Bugakov VI, Dub SN, Kurakevych OO, Kondrin MV, et al. Bulk nanostructured carbon phases prepared from C-60: approaching the 'ideal' hardness. *Journal of Physics-Condensed Matter*. 2007;19(23). doi:10.1088/0953-8984/19/23/236209
- [107] Baimova JA, Korznikova EA, Dmitriev SV, Liu B, Zhou K. REVIEW ON CRUMPLED GRAPHENE: UNIQUE MECHANICAL PROPERTIES. *Reviews on Advanced Materials Science*. 2014;39(1):69-83.

- [108] Marks N. Modelling diamond-like carbon with the environment-dependent interaction potential. *Journal of Physics-Condensed Matter*. 2002;14(11):2901-27. doi:10.1088/0953-8984/14/11/308
- [109] Powles RC, Marks NA, Lau DWM. Self-assembly of sp(2)-bonded carbon nanostructures from amorphous precursors. *Physical Review B*. 2009;79(7). doi:10.1103/PhysRevB.79.075430
- [110] Suarez-Martinez I, Marks NA. Effect of microstructure on the thermal conductivity of disordered carbon. *Applied Physics Letters*. 2011;99(3). doi:10.1063/1.3607872
- [111] Daniele SAB, Boulfefel SE, Schapotschnikow P, Donadio D, Leoni S. Hierarchical thermoelectrics: crystal grain boundaries as scalable phonon scatterers. *Nanoscale*. 2016;8(6):3729-38. doi:10.1039/c5nr05279c
- [112] Zhu DM. THERMAL-CONDUCTIVITY OF DENSIFIED ALPHA-SIO2 FROM 15-5 TO ROOM-TEMPERATURE. *Physical Review B*. 1994;50(9):6053-6. doi:10.1103/PhysRevB.50.6053
- [113] Inamura Y, Arai M, Yamamuro O, Inaba A, Kitamura N, Otomo T, et al. Peculiar suppression of the specific heat and boson peak intensity of densified SiO2 glass. *Physica B*. 1999;263:299-302. doi:10.1016/s0921-4526(98)01362-3
- [114] Liu X, Loehneysen V, Weiss G, Arndt J. Low-temperature specific heat of compacted vitreous silica. *Zeitschrift Fur Physik B-Condensed Matter*. 1995;99(1):49-55. doi:10.1007/s002570050009
- [115] Grace JM, Anderson AC. LOW-TEMPERATURE THERMAL-PROPERTIES OF A SOL-GEL GLASS. *Physical Review B*. 1986;33(10):7186-91. doi:10.1103/PhysRevB.33.7186
- [116] Yang LN, Yang N, Li BW. Reduction of Thermal Conductivity by Nanoscale 3D Phononic Crystal. *Scientific Reports*. 2013;3. doi:10.1038/srep01143
- [117] Graebner JE, Reiss ME, Seibles L, Hartnett TM, Miller RP, Robinson CJ. PHONON-SCATTERING IN CHEMICAL-VAPOR-DEPOSITED DIAMOND. *Physical Review B*. 1994;50(6):3702-13. doi:10.1103/PhysRevB.50.3702
- [118] Wang Y, Fujinami K, Zhang R, Wan C, Wang N, Ba Y, et al. Interfacial Thermal Resistance and Thermal Conductivity in Nanograined SrTiO3. *Applied Physics Express*. 2010;3(3). doi:10.1143/apex.3.031101
- [119] Wang Z, Alaniz JE, Jang W, Garay JE, Dames C. Thermal Conductivity of Nanocrystalline Silicon: Importance of Grain Size and Frequency-Dependent Mean Free Paths. *Nano Letters*. 2011;11(6):2206-13. doi:10.1021/nl1045395
- [120] Zhang Y, Mehta RJ, Belley M, Han L, Ramanath G, Borca-Tasciuc T. Lattice thermal conductivity diminution and high thermoelectric power factor retention in nanoporous macroassemblies of sulfur-doped bismuth telluride nanocrystals. *Applied Physics Letters*. 2012;100(19). doi:10.1063/1.4711774
- [121] Mingo N, Hauser D, Kobayashi NP, Plissonnier M, Shakouri A. "Nanoparticle-in-Alloy" Approach to Efficient Thermoelectrics: Silicides in SiGe. *Nano Letters*. 2009;9(2):711-5. doi:10.1021/nl8031982
- [122] Belay K, Etzel ZY, Onn DG, Anthony TR. The thermal conductivity of polycrystalline diamond films: Effects of isotope content. *Journal of Applied Physics*. 1996;79(11):8336-40. doi:10.1063/1.362546
- [123] Uma S, McConnell AD, Ashghi M, Kurabayashi K, Goodson KE. Temperature-dependent thermal conductivity of undoped polycrystalline silicon layers. *Int J Thermophys*. 2001;22(2):605-16. doi:10.1023/a:1010791302387
- [124] Khafizov M, Park I-W, Chernatynskiy A, He L, Lin J, Moore JJ, et al. Thermal Conductivity in Nanocrystalline Ceria Thin Films. *Journal of the American Ceramic Society*. 2014;97(2):562-9. doi:10.1111/jace.12673
- [125] Bodapati A, Koblinski P, Schelling PK, Phillpot SR. Crossover in thermal transport mechanism in nanocrystalline silicon. *Applied Physics Letters*. 2006;88(14). doi:10.1063/1.2192145
- [126] Damart T, Giordano VM, Tanguy A. Nanocrystalline inclusions as a low-pass filter for thermal transport in a-Si. *Physical Review B*. 2015;92(9). doi:10.1103/PhysRevB.92.094201
- [127] Elliott SR. A UNIFIED MODEL FOR THE LOW-ENERGY VIBRATIONAL BEHAVIOR OF AMORPHOUS SOLIDS. *Europhysics Letters*. 1992;19(3):201-6. doi:10.1209/0295-5075/19/3/009
- [128] Stanke FE, Kino GS. A UNIFIED THEORY FOR ELASTIC WAVE-PROPAGATION IN POLYCRYSTALLINE MATERIALS. *Journal of the Acoustical Society of America*. 1984;75(3):665-81. doi:10.1121/1.390577
- [129] Klemens PG. PHONON-SCATTERING AND THERMAL-RESISTANCE DUE TO GRAIN-BOUNDARIES. *Int J Thermophys*. 1994;15(6):1345-51. doi:10.1007/bf01458842
- [130] Kim W, Majumdar A. Phonon scattering cross section of polydispersed spherical nanoparticles. *Journal of Applied Physics*. 2006;99(8). doi:10.1063/1.2188251

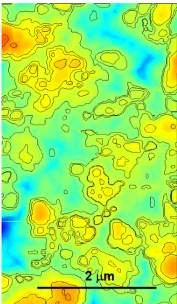
- [131] Nomura M, Kage Y, Nakagawa J, Hori T, Maire J, Shiomi J, et al. Impeded thermal transport in Si multiscale hierarchical architectures with phononic crystal nanostructures. *Physical Review B*. 2015;91(20). doi:10.1103/PhysRevB.91.205422
- [132] Tondi G, Fierro V, Pizzi A, Celzard A. Tannin-based carbon foams. *Carbon*. 2009;47(6):1480-92. doi:10.1016/j.carbon.2009.01.041
- [133] Baldi G, Giordano VM, Monaco G, Ruta B. Sound Attenuation at Terahertz Frequencies and the Boson Peak of Vitreous Silica. *Physical Review Letters*. 2010;104(19). doi:10.1103/PhysRevLett.104.195501
- [134] Rupp J, Birringer R. ENHANCED SPECIFIC-HEAT-CAPACITY (CP) MEASUREMENTS (150-300 K) OF NANOMETER-SIZED CRYSTALLINE MATERIALS. *Physical Review B*. 1987;36(15):7888-90. doi:10.1103/PhysRevB.36.7888
- [135] Tan ZC, Wang L, Shi Q. Study of heat capacity enhancement in some nanostructured materials. *Pure and Applied Chemistry*. 2009;81(10):1871-80. doi:10.1351/pac-con-08-09-15
- [136] Wagner M. STRUCTURE AND THERMODYNAMIC PROPERTIES OF NANOCRYSTALLINE METALS. *Physical Review B*. 1992;45(2):635-9. doi:10.1103/PhysRevB.45.635
- [137] Rojas DP, Barquin LF, Fernandez JR, Fernandez LR, Gonzalez J. Phonon softening on the specific heat of nanocrystalline metals. *Nanotechnology*. 2010;21(44). doi:10.1088/0957-4484/21/44/445702
- [138] Chen YY, Yao YD, Hsiao SS, Jen SU, Lin BT, Lin HM, et al. SPECIFIC-HEAT STUDY OF NANOCRYSTALLINE PALLADIUM. *Physical Review B*. 1995;52(13):9364-9. doi:10.1103/PhysRevB.52.9364
- [139] Bai HY, Luo JL, Jin D, Sun JR. Particle size and interfacial effect on the specific heat of nanocrystalline Fe. *Journal of Applied Physics*. 1996;79(1):361-4. doi:10.1063/1.360838
- [140] Tamura A, Higeta K, Ichinokawa T. LATTICE-VIBRATIONS AND SPECIFIC-HEAT OF A SMALL PARTICLE. *Journal of Physics C-Solid State Physics*. 1982;15(24):4975-91. doi:10.1088/0022-3719/15/24/010
- [141] Montagna M, Dusi R. RAMAN-SCATTERING FROM SMALL SPHERICAL-PARTICLES. *Physical Review B*. 1995;52(14):10080-9. doi:10.1103/PhysRevB.52.10080
- [142] Duval E, Boukenter A, Champagnon B. VIBRATION EIGENMODES AND SIZE OF MICROCRYSTALLITES IN GLASS - OBSERVATION BY VERY-LOW-FREQUENCY RAMAN-SCATTERING. *Physical Review Letters*. 1986;56(19):2052-5. doi:10.1103/PhysRevLett.56.2052
- [143] Fujii M, Kanzawa Y, Hayashi S, Yamamoto K. Raman scattering from acoustic phonons confined in Si nanocrystals. *Physical Review B*. 1996;54(12):R8373-R6.
- [144] Wolf D, Wang J, Phillpot SR, Gleiter H. PHONON-INDUCED ANOMALOUS SPECIFIC-HEAT OF A NANOCRYSTALLINE MODEL MATERIAL BY COMPUTER-SIMULATION. *Physical Review Letters*. 1995;74(23):4686-9. doi:10.1103/PhysRevLett.74.4686
- [145] Phillips WA. Tunneling states in amorphous solids. *J Low Temp Phys*. 1972;7(3-4):351-60. doi:10.1007/BF00660072
- [146] Anderson PW, Halperin BI, Varma CM. ANOMALOUS LOW-TEMPERATURE THERMAL PROPERTIES OF GLASSES AND SPIN GLASSES. *Philosophical Magazine*. 1972;25(1):1-&. doi:10.1080/14786437208229210
- [147] Cano A, Levanyuk AP. Low-temperature specific heat of real crystals: Possibility of leading contribution of optical vibrations and short-wavelength acoustical vibrations. *Physical Review B*. 2004;70(21). doi:10.1103/PhysRevB.70.212301
- [148] Cano A, Levanyuk AP. Explanation of the glasslike anomaly in the low-temperature specific heat of incommensurate phases. *Physical Review Letters*. 2004;93(24). doi:10.1103/PhysRevLett.93.245902
- [149] Taraskin SN, Elliott SR. Nature of vibrational excitations in vitreous silica. *Physical Review B*. 1997;56(14):8605-22. doi:10.1103/PhysRevB.56.8605
- [150] Allen PB, Feldman JL. THERMAL-CONDUCTIVITY OF DISORDERED HARMONIC SOLIDS. *Physical Review B*. 1993;48(17):12581-8. doi:10.1103/PhysRevB.48.12581
- [151] Feldman JL, Allen PB, Bickham SR. Numerical study of low-frequency vibrations in amorphous silicon. *Physical Review B*. 1999;59(5):3551-9. doi:10.1103/PhysRevB.59.3551
- [152] Taraskin SN, Elliott SR. Ioffe-Regel crossover for plane-wave vibrational excitations in vitreous silica. *Physical Review B*. 2000;61(18):12031-7. doi:10.1103/PhysRevB.61.12031
- [153] Beltukov YM, Kozub VI, Parshin DA. Ioffe-Regel criterion and diffusion of vibrations in random lattices. *Physical Review B*. 2013;87(13). doi:10.1103/PhysRevB.87.134203

- [154] Pilla O, Caponi S, Fontana A, Concalves JR, Montagna M, Rossi F, et al. The low energy excess of vibrational states in  $v$ -SiO<sub>2</sub>: the role of transverse dynamics. *Journal of Physics-Condensed Matter*. 2004;16(47):8519-30. doi:10.1088/0953-8984/16/47/006
- [155] Mizuno H, Mossa S, Barrat J-L. Elastic heterogeneity, vibrational states, and thermal conductivity across an amorphisation transition. *Epl*. 2013;104(5). doi:10.1209/0295-5075/104/56001
- [156] Marruzzo A, Schirmacher W, Fratallocchi A, Ruocco G. Heterogeneous shear elasticity of glasses: the origin of the boson peak. *Scientific Reports*. 2013;3. doi:10.1038/srep01407
- [157] Taraskin SN, Elliott SR. Vector vibrations and the Ioffe-Regel crossover in disordered lattices. *Journal of Physics-Condensed Matter*. 2002;14(12):3143-66. doi:10.1088/0953-8984/14/12/306
- [158] Schirmacher W. Thermal conductivity of glassy materials and the "boson peak". *Europhysics Letters*. 2006;73(6):892-8. doi:10.1209/epl/i2005-10471-9
- [159] Schirmacher W, Ruocco G, Scopigno T. Acoustic attenuation in glasses and its relation with the boson peak. *Physical Review Letters*. 2007;98(2). doi:10.1103/PhysRevLett.98.025501
- [160] Mizuno H, Mossa S, Barrat J-L. Acoustic excitations and elastic heterogeneities in disordered solids. *Proceedings of the National Academy of Sciences of the United States of America*. 2014;111(33):11949-54. doi:10.1073/pnas.1409490111
- [161] Tanguy A, Wittmer JP, Leonforte F, Barrat JL. Continuum limit of amorphous elastic bodies: A finite-size study of low-frequency harmonic vibrations. *Physical Review B*. 2002;66(17). doi:10.1103/PhysRevB.66.174205
- [162] Leonforte F, Boissiere R, Tanguy A, Wittmer JP, Barrat JL. Continuum limit of amorphous elastic bodies. III. Three-dimensional systems. *Physical Review B*. 2005;72(22). doi:10.1103/PhysRevB.72.224206
- [163] Leonforte F, Tanguy A, Wittmer JP, Barrat JL. Inhomogeneous elastic response of silica glass. *Physical Review Letters*. 2006;97(5). doi:10.1103/PhysRevLett.97.055501
- [164] Mizuno H, Mossa S, Barrat JL. Measuring spatial distribution of the local elastic modulus in glasses. *Physical Review E*. 2013;87(4). doi:10.1103/PhysRevE.87.042306
- [165] Reinisch J, Heuer A. What is moving in silica at 1 k? A computer study of the low-temperature anomalies. *Physical Review Letters*. 2005;95(15). doi:10.1103/PhysRevLett.95.155502
- [166] Trachenko K, Turlakov M. Tunneling and interaction effects in two-level systems in glasses studied by atomistic simulations. *Physical Review B*. 2006;73(1). doi:10.1103/PhysRevB.73.012203
- [167] Tsamados M, Tanguy A, Goldenberg C, Barrat J-L. Local elasticity map and plasticity in a model Lennard-Jones glass. *Physical Review E*. 2009;80(2). doi:10.1103/PhysRevE.80.026112
- [168] Tanguy A, Mantsi B, Tsamados M. Vibrational modes as a predictor for plasticity in a model glass. *Epl*. 2010;90(1). doi:10.1209/0295-5075/90/16004

Scanning acoustic microscopy



Atomic force microscopy



Scanning tunneling microscopy

